INTERFEOMETRY DATA CALIBRATION AND IMAGE PROCESSING

SHUBHENDU JOARDAR

B.Tech. (Electronics, NIT Calicut)

M.S. (Microwaves, IIT Madras)

F.I.E.T.E. (IETE, India)

Ph.D. (Physics, University of Kalyani)

License

Introduction

The ultimate goal of radio interferometry is to construct the images of astronomical radio sources. The process broadly involves three steps:

(i) Data sorting.
(ii) Data calibration.
(iii) Construction of image.

Data sorting involves removal of those data which are affected by instrumental problems and RFI, etc. Data calibration is necessary to free it from instrumental gain and phase contributions. Image construction involves a transformation and a lot of post processing to improve the image quality. Here we discuss about calibration and construction of image.

In previous chapter we studied the van Cittert-Zernike equation in details which forms the base of image construction. We now investigate how to apply this in image construction in more details.

Basic Ideas of Image Construction-I

Let an extended quasi-monochromatic source be observed. The u,v,w coordinates measure the projections of d_λ. The w-axis always point towards the phase reference point of the source. The brightness distribution $I(l,m)$ on the celestial sphere is a function of the direction cosines l, m and n. The interferometer response (spatial coherence function $\mathcal{V}(u,v,w)$) can be expressed using the van Cittert-Zernike equation as:

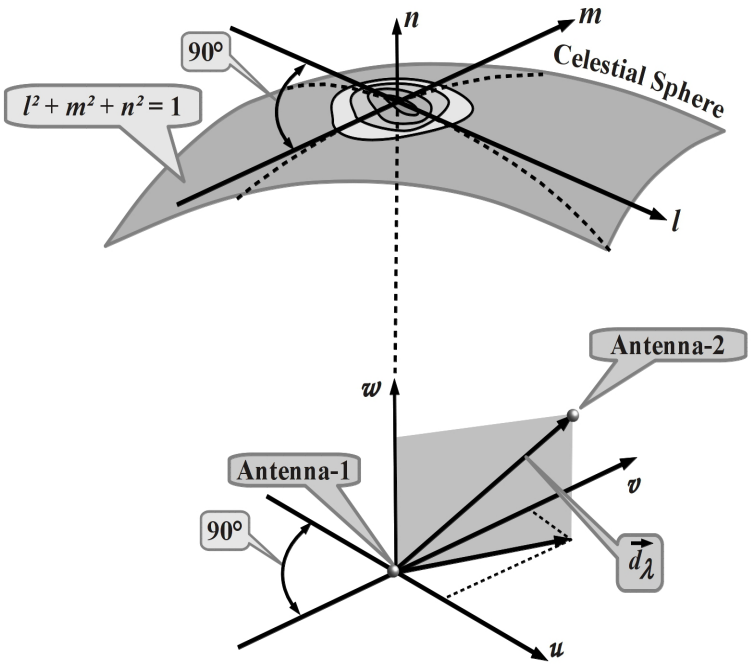

$$\mathcal{V}(u,v,w) = \int_{-\infty}^{\infty}\int_{-\infty}^{\infty} \frac{P_n(l,m)\, I(l,m)}{n}\, e^{-j2\pi[ul+vm+w(n-1)]}\, dl\, dm \quad \ldots (1)$$

Here, $P_n(l,m)$ is the normalized primary beam pattern of an antenna and n is given as: $n = \sqrt{1-l^2-m^2}$

Eq. (1) shows that $\mathcal{V}(u,v,w)$ is a Fourier-like integral of the product of (*i*) $I(l,m)$, (*ii*) normalized primary beam pattern $P_n(l,m)$, and (*iii*) $1/n$. It can be used directly for imaging, especially when the source extents are large. This kind of imaging is generally called ***wide-field imaging***.

Basic Ideas of Image Construction-II

For very small sources observed with interferometers having narrow primary beam-widths it is convenient to assume (*i*) $n \approx 1$ and (*ii*) $P_n(l,m) \approx 1$. This reduces the complexity of computation since the van Cittert-Zernike equation becomes independent of n and w as:

$$\mathcal{V}(u,v) = \int_{-\infty}^{\infty}\int_{-\infty}^{\infty} I(l,m)\, \exp\left[-j2\pi\,(lu+mv)\right]\, dl\, dm \quad \ldots (2)$$

This approximation $P_n(l,m) \approx 1$ makes it impossible to image large fields. Some effects may be corrected in the final stages of image analysis. This two dimensional relationship has been widely used and we shall call it as ***conventional imaging***. Recent researchers are devising ways to avoid these approximations for allowing imaging larger fields. Interferometer arrays contains more then two antennas and have several different baselines. The number of baselines is ${}^{N}\mathrm{C}_{2}$, where N is the number of antennas. An interferometer array aided by super-synthesis gives a good amount of data in the u,v,w domain.

We begin with the study of general calibration techniques and then we move on to the conventional imaging techniques (for small fields of view). Towards the end we show some techniques of wide-field imaging. Finally we shall talk about spectral line observations.

Long Term Calibration Techniques

General Calibration Techniques

The interferometer data contain system dependent terms. These are different for different antennas. The receiving systems may introduce extra gain and phase. These variations can be long or short. Hence the calibration processes are broadly of two types: (*i*) long term, and (*ii*) short term calibrations.

Long Term Calibration

Due to the self weights of the antenna structures, mechanical deformations may take place. These are elastic in nature and position dependent. These include:

(*i*) Antenna coordinates and baselines.

(*ii*) Antenna pointing corrections caused from miss-alignments.

Calibrations for above problems are generally done every week and also before observing the target source. A radio source of known flux-density is generally used for this purpose. The antennas are pointed to this source and the zero points are set in such a way that delays from antennas to correlator are same for all. These settings are expected to function throughout the actual observation period.

Short Term Calibration Techniques-I

- Short term calibrations are done intermittently within the observation period. A point radio source with known flux-density which is located in a direction close to the target source is generally used. The calibration data is recorded side by side with the target source data. The calibration data is applied during data analysis (after observation). However, the visibility data must be carefully edited before applying these, so that the data is free from any evidence of equipment malfunctioning or traces of radio interference. The data is examined for any un-expected level of gain and phase variations. These are eliminated by a process called ***flagging***.

- Short term calibrations are made to correct the gain and phase of the telescope which includes antenna and the correlator. Phase corrections are important for eliminating the phase fluctuations caused by changing ionospheric behavior, especially at frequencies below 1 GHz. It increases with the wavelength size. These are also important for correcting the constant component of atmospheric attenuation which changes as we move away from the zenith.

Short Term Calibration Techniques-II

- Other problems like shadowing of one antenna by any other antenna when the projected baselines become small at lower elevation angles can be overcome by short term calibrations. Due to ground temperature pickup by antenna-feed spill-over, mesh leakage and side-lobes, the system noise temperature changes with antenna elevation. This may cause the ALC (automatic level control) to change the system gain, which is used in many telescopes. Receiving system can be checked intermittently by injecting a known quantity of noise into the receiver (using a directional coupler near the LNA) and observing its effect at the correlator output.

- Instead of a calibrated radio astronomical source whose position and power are known, a more recent technique called ***self-calibration*** may be used. For VLBI observations, additional steps are required for matching time, phase and frequency of different observatory data.

Radio Sources as Calibrators-I

We know that... $$\mathcal{V}(u,v) = \int_{-\infty}^{\infty}\int_{-\infty}^{\infty} I(l,m)\,\exp\left[-j2\pi\,(lu+mv)\right]\,dl\,dm \quad \ldots (2)$$

Let $G_{mn}(t)$ be the factor by which the system gain of an interferometer (consisting of antennas m and n) changes as a function of observation time. Let $\mathcal{V}_{\text{uc}}(u,v)$ represent the uncalibrated visibility. Eq. (2) can be combined with $G_{mn}(t)$ and the uncalibrated interferometer response can be written as:

$$\mathcal{V}_{\text{uc}}(u,v) = G_{mn}(t)\int_{-\infty}^{\infty}\int_{-\infty}^{\infty} I(l,m)\,e^{-j2\pi[ul+vm]}dl\,dm \quad \ldots (3)$$

The complex gain factor $G_{mn}(t)$ is a function of gain parameters of antennas m and n forming the interferometer. It varies with time. Comparing Eq. (3) with Eq. (2) we express $\mathcal{V}_{\text{uc}}(u,v)$ as:

$$\mathcal{V}_{\text{uc}}(u,v) = G_{mn}(t)\mathcal{V}(u,v) \quad \ldots (4)$$

When the interferometer is pointed to an unresolved calibrator source of know flux-density S_c (watt/m^2/Hz) such that the source is located at the phase center of its field, the measured visibility $\mathcal{V}_c(u,v)$ is given as:

$$\mathcal{V}_c(u,v) = G_{mn}\,S_c \quad \ldots (5)$$

Comparing Eq. (4) with (5) we get: $$\mathcal{V}(u,v) = \mathcal{V}_{\text{uc}}(u,v)\left(\frac{S_c}{\mathcal{V}_c(u,v)}\right) \quad \ldots (6)$$

Radio Sources as Calibrators-II

Eq. (5) gives the amplitude $|G_{mn}|$ and phase $\angle G_{mn}$ of $G_{mn}(t)$ respectively as:

$$|G_{mn}| = \left|\frac{\mathcal{V}_c}{S_c}\right| \quad \ldots (7) \qquad \angle G_{mn} = \angle\left(\mathcal{V}_c / S_c\right) \quad \ldots (8)$$

We may express the gain factor G_{mn} using Eqs. (7) and (8) in terms of amplitude and phase as:

$$G_{mn} = |G_{mn}|\, e^{j\angle G_{mn}} = \left|\frac{\mathcal{V}_c}{S_c}\right| e^{j\angle(\mathcal{V}_c/S_c)} \quad \ldots (9)$$

The instrumental gain factor G_{mn}, visibility $\mathcal{V}$ and the uncalibrated visibility $\mathcal{V}_{\text{uc}}$ after representing in their magnitude and phase form can be related as:

$$\mathcal{V} = |\mathcal{V}|\, e^{j\angle\mathcal{V}} = \frac{|\mathcal{V}_{\text{uc}}|\, e^{j\angle\mathcal{V}_{\text{uc}}}}{|G_{mn}|\, e^{j\angle G_{mn}}} = \left|\frac{\mathcal{V}_{\text{uc}}}{G_{mn}}\right| e^{j(\angle\mathcal{V}_{\text{uc}} - \angle G_{mn})} \quad \ldots (10)$$

It is seen from Eq. (10) that the magnitude of the visibility $\mathcal{V}$ is a ratio of magnitudes of the uncalibrated visibility $\mathcal{V}_{\text{uc}}$ to that of instrumental gain factor G_{mn}. Again, the phase of the visibility $\mathcal{V}$ is the phase of the uncalibrated visibility $\mathcal{V}_{\text{uc}}$ minus the phase of G_{mn}. These are:

$$|\mathcal{V}| = \frac{|\mathcal{V}_{\text{uc}}|}{|G_{mn}|} = \left|\frac{\mathcal{V}_{\text{uc}}\, S_c}{\mathcal{V}_c}\right| \quad \ldots (11) \qquad \angle\mathcal{V} = \angle\mathcal{V}_{\text{uc}} - \angle G_{mn} = \angle\mathcal{V}_{\text{uc}} - \angle\left(\mathcal{V}_c / S_c\right) \quad \ldots (12)$$

Radio Sources as Calibrators-III

Notes:

Calibrations for both polarizations must be separately performed. It is preferable to perform gain calibrations immediately before the actual observation by means of a high power unresolved calibrator source. Phase calibrations are intermittently performed throughout the observation period by interrupting the target observation process and move to an unresolved phase calibrator source lying in a direction very close to the target. This allows the telescope to make use of almost identical ionosphere medium present between the target source and the antennas so as to detect correct phase variations. As mentioned before, the instrumental phase obtained using the calibrator must be subtracted from the phase of the target visibility. Gain calibrators must be strong for obtaining good SNR within short time. Strong sources are few in number, and may not be always available close to the target source. Hence, separate calibrators for gain and phase are used.

Commonly used gain or flux calibrators are 3C48, 3C147, 3C286 and 3C295. Thermal sources like compact planetary nebula NGC7027 can be very useful for short baselines.

Self Calibration-I

Self-calibration is based on (*i*) phase closure and (*ii*) gain closure obtained from a few antennas. The target source being observed is used as a calibrator. Though there are different gain pairs G_{mn} formed from different antenna pairs, still the data contain good observables. For an array of N antennas, $N(N\text{-}1)/2$ baselines are formed which is equal to number of visibilities obtained at any instant. We express $G_{mn} = g_m\, g_n^*$, where g_m and g_n are respectively the complex gain factors of signal paths associated with antennas m and n. Hence there are N unknown complex antenna gain factors g_m, which means N unknown amplitude factors and N unknown phases. Thus there are $[N(N\text{-}1)/2]$ - N uncorrupted complex quantities due to antenna effects which are called closure quantities as we see shall see next.

Phase closure: It is the sum of visibility phases around a triangle formed using three antennas. Let the antenna pairs pq, qr and rp respectively give the calibrated visibilities $\mathcal{V}^{pq}$, $\mathcal{V}^{qr}$ and $\mathcal{V}^{rp}$. Let the corresponding uncalibrated visibilities be $\mathcal{V}^{pq}{}_{\text{uc}}$, $\mathcal{V}^{qr}{}_{\text{uc}}$ and $\mathcal{V}^{rp}{}_{\text{uc}}$ respectively. Then, at any instant of time, the sum of phases of calibrated visibilities is equal to the sum of phases of uncalibrated visibilities:

$$\angle\mathcal{V}^{pq} + \angle\mathcal{V}^{qr} + \angle\mathcal{V}^{rp} = \angle\mathcal{V}^{pq}_{\text{uc}} + \angle\mathcal{V}^{qr}_{\text{uc}} + \angle\mathcal{V}^{rp}_{\text{uc}} \qquad \ldots (13)$$

Self Calibration-II

Gain closure: The gain closure requires a minimum of four antennas. Let these four antennas be p, q, r and s. It can be shown that gain magnitudes of uncalibrated and calibrated visibilities are given as:

$$A_{pqrs} = \frac{|\mathcal{V}^{pq}_{\rm uc}|\,|\mathcal{V}^{rs}_{\rm uc}|}{|\mathcal{V}^{pr}_{\rm uc}|\,|\mathcal{V}^{qs}_{\rm uc}|} = \frac{|\mathcal{V}^{pq}|\,|\mathcal{V}^{rs}|}{|\mathcal{V}^{pr}|\,|\mathcal{V}^{qs}|} \quad \ldots (14)$$

Three different gain closures (A_{pqrs}, A_{pqsr}, A_{qrsp}) can be calculated if all six interferometers formed are correlated, but only two of these are independent.

Before starting the actual observation, a set of data is taken. This is calibrated from current best estimate of the antenna gains and a model of the sky is generated using imaging techniques. Considering this sky model as correct, visibilities are obtained by which new antenna gains are found that reduces the difference between model and measured visibilities. Let $\mathcal{V}^{pq}{}_{\rm mod}$ and $\mathcal{V}^{pq}{}_{\rm uc}$ respectively represent the model and measured (uncalibrated) visibilities. Assuming $\mathcal{V}^{pq}{}_{\rm uc} = G_{pq}\mathcal{V}^{pq}{}_{\rm mod}$ from Eq. (4), the quantity ε^2 shown below has to be minimized to obtain the values of g_p, g_q and G_{pq}. Actual observations are made with these calibrated values. It is assumed that these gain solutions remain valid over entire observation.

$$\epsilon^2 = \sum_{p,q} \left| \mathcal{V}^{pq}_{\rm mod} - \frac{\mathcal{V}^{pq}_{\rm uc}}{g_p\, g^{\star}_q} \right|^2 \quad \ldots (15)$$

Additional Self-Calibration Techniques-I

Certain techniques can be used to aid self-calibrations. Two are of them are commonly used which are described next.

Self-calibration with redundant array: An array is designed to measure a common Fourier component of a brightness distribution using more than one baseline. It is called a redundant array since some of the baselines are identical. An example of a redundant array of five antennas is shown. The antennas are separated over a a distance d. The total number of baselines is 10. The various baselines and their redundancies are listed in Table below.

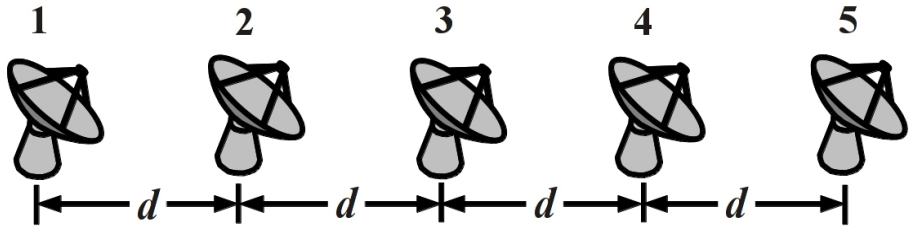

Antenna Pairs	Baseline Length	No. of Baselines
1-2, 2-3, 3-4, 4-5	d	4 (redundant)
1-3, 2-4, 3-5	$2d$	3 (redundant)
1-4, 2-5	$3d$	2 (redundant)
1-5	$4d$	1

By substituting $G_{mn} = g_m\, g_n^*$ in Eq. (4), the uncalibrated visibility $\mathcal{V}^{mn}{}_{\text{uc}}$ can be shown in terms of the true visibility $\mathcal{V}^{mn}$ as:

$$\mathcal{V}^{mn}_{\text{uc}}(u,v) = \mathcal{V}^{mn}(u,v)\, g_m g_n^*, \text{ or } \mathcal{V}^{mn}(u,v)\, g_m^* g_n \quad \ldots (16)$$

Additional Self-Calibration Techniques-II

The equations obtained using baselines of length d from the redundant array are shown as:

$$\begin{bmatrix} \mathcal{V}_{\rm uc}^{1,2} \\ \mathcal{V}_{\rm uc}^{2,3} \\ \mathcal{V}_{\rm uc}^{3,4} \\ \mathcal{V}_{\rm uc}^{4,5} \end{bmatrix} = \begin{bmatrix} \mathcal{V}^{1,2}\, g_1\, g_2^* \\ \mathcal{V}^{2,3}\, g_2^* g_3 \\ \mathcal{V}^{3,4}\, g_3\, g_4^* \\ \mathcal{V}^{4,5}\, g_4^* g_5 \end{bmatrix} \quad \ldots (17)$$

For the baselines having $2d$ spacings we obtain:

$$\begin{bmatrix} \mathcal{V}_{\rm uc}^{1,3} \\ \mathcal{V}_{\rm uc}^{2,4} \\ \mathcal{V}_{\rm uc}^{3,5} \end{bmatrix} = \begin{bmatrix} \mathcal{V}^{1,3}\, g_1\, g_3^* \\ \mathcal{V}^{2,4}\, g_2\, g_4^* \\ \mathcal{V}^{3,5}\, g_3^* g_5 \end{bmatrix} \quad \ldots (18)$$

For the baselines having $3d$ spacings we obtain:

$$\begin{bmatrix} \mathcal{V}_{\rm uc}^{1,4} \\ \mathcal{V}_{\rm uc}^{2,5} \end{bmatrix} = \begin{bmatrix} \mathcal{V}^{1,4}\, g_1\, g_4^* \\ \mathcal{V}^{2,5}\, g_2^* g_5 \end{bmatrix} \quad \ldots (19)$$

Solving the above equations we obtain the complex gain ratios as:

$$\begin{bmatrix} g_1/g_3 \\ g_2/g_4 \\ g_3/g_5 \\ g_5/g_1 \end{bmatrix} = \begin{bmatrix} \mathcal{V}_{\rm uc}^{1,2}/\mathcal{V}_{\rm uc}^{2,3} \\ \left(\mathcal{V}_{\rm uc}^{2,3}/\mathcal{V}_{\rm uc}^{3,4}\right)^* \\ \mathcal{V}_{\rm uc}^{3,4}/\mathcal{V}_{\rm uc}^{4,5} \\ \mathcal{V}_{\rm uc}^{3,5}/\mathcal{V}_{\rm uc}^{1,3} \end{bmatrix} \quad \ldots (20)$$

It may be possible to estimate the individual antenna gains from a standard map or if one the antenna gains is known. The main drawback of using redundant array comes from reduced u-v coverage, since common data sets are generated.

Additional Self-Calibration Techniques-III

Self-calibration using redundant data (cross-overs in *u-v* plane): If an interferometer array have North-South baseline components, the observed data may contain repetitions (redundancy) of same spatial frequency components produced by different interferometers as shown on right. The redundant data is encircled in the picture which may be used for calibration.

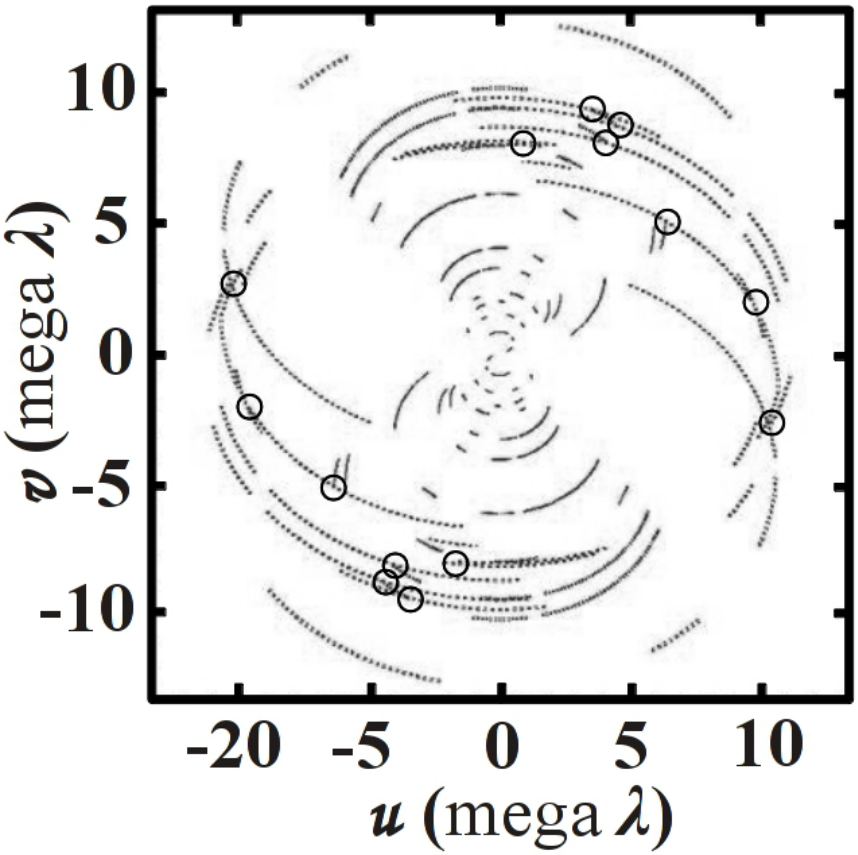

Self-calibration work well for strong sources, or when the SNR in the visibility data is reasonably good. Though both phase and gain calibrations are required, the former is more effective and can be accurately done by self-calibration. As a precautionary note, self-calibration using low SNR visibility data can result artifacts in the image.

Conventional Imaging Method-I

The van Cittert-Zernike equation (Eq. (2)) is reproduced below:

$$\mathcal{V}(u,v) = \int_{-\infty}^{\infty}\int_{-\infty}^{\infty} I(l,m)\,\exp\left[-j2\pi\left(lu+mv\right)\right]\,dl\,dm \quad \ldots (2)$$

It forms the basis of conventional imaging. Images are made only after calibrating the good visibility data. There are two steps involved:

(*i*) Creating the best possible image (called ***dirty image***) from the data by applying weighting techniques.

(*ii*) Improving the quality of the dirty image by certain image processing functions like ***deconvolution***.

We start by constructing a dirty image with assumption that the visibility data is already calibrated for gain and phase. We know that the measured and calibrated visibility $\mathcal{V}_{\rm mc}(u,v)$ is a product of true visibility $\mathcal{V}(u,v)$ and the spatial sensitivity function $W(u,v)$ given as:

$$\mathcal{V}_{\rm mc}(u.v) = \mathcal{V}(u,v)\,W(u,v) \quad \ldots (21)$$

Conventional Imaging Method-II

From previous slide ….

$$\mathcal{V}_{\rm mc}(u.v) = \mathcal{V}(u,v)\, W(u,v) \quad \text{... (21)}$$

The data is now scaled called ***weighting*** whose reasons will be clear later. The measured calibrated and weighted visibilities $\mathcal{V}_{\rm mcw}(u,v)$ is expressed below, where $w(u,v)$ is the weighting function.

$$\mathcal{V}_{\rm mcw}(u,v) = \mathcal{V}(u,v)\, W(u,v)\, w(u,v) \quad \text{... (22)}$$

An inverse Fourier transform recovers the sky brightness distribution $I(l,m)$ as shown in Eq. (2). Applying this to Eq. (22) from both sides we obtain:

$$I_{\rm mcw}(l,m) = I(l,m) \star P_{\rm syn}(l,m) \quad \text{... (23)}$$

Here $I_{\rm mcw}(l,m)$ represents a distorted source intensity distribution resulting from the synthesized beam pattern, and $P_{\rm syn}(l,m)$ represents the synthesized beam pattern. The symbol $*$ represents convolution. We may expand these terms as shown in three equations.

Conventional Imaging Method-III

$$I_{\mathrm{mcw}}(l,m) = \int_{-\infty}^{\infty}\int_{-\infty}^{\infty} \mathcal{V}_{\mathrm{mcw}}(u,v)\, e^{j2\pi(lu+mv)}\, du\, dv \qquad \ldots (24)$$

$$I(l,m) = \int_{-\infty}^{\infty}\int_{-\infty}^{\infty} \mathcal{V}(u,v)\, e^{j2\pi(lu+mv)}\, du\, dv \qquad \ldots (25)$$

$$P_{\mathrm{syn}}(l,m) = \int_{-\infty}^{\infty}\int_{-\infty}^{\infty} W(u,v)\, w(u,v)\, e^{j2\pi(lu+mv)}\, du\, dv \qquad \ldots (26)$$

Note: We can modify the synthesized beam $P_{\mathrm{syn}}(l,m)$ by changing the weights $w(u,v)$. The interferometer does not give a continuous distribution of visibility across the u-v plane. Instead, it appears at a discrete set of points u_i, v_i, where i is an integer. It contains an ensemble of N_{vis} pair of points which appear symmetrically on both sides of the origin of the u,v axes. The dirty image $I_{\mathrm{D}}(l,m)$ is expressed in discrete form as:

$$I_{\mathrm{D}}(l,m) = \sum_{i=1}^{N_{vis}} w_i \left[\mathcal{V}_{\mathrm{mc}}(u_i,v_i)\, e^{j2\pi(lu_i+mv_i)} + \mathcal{V}_{\mathrm{mc}}(-u_i,-v_i)\, e^{-j2\pi(lu_i+mv_i)}\right] \quad \ldots (27)$$

Conventional Imaging Method-IV

Let both antennas have identical polarizations. The measured-calibrated visibilities on both sides of the origin of u,v coordinates form a complex conjugate pair as shown below:

$$\mathcal{V}_{\rm mc}(-u_i,-v_i) = \mathcal{V}^{\star}_{\rm mc}(u_i,v_i)\,, \quad i = 1,2,...,N_{\rm vis} \qquad ... (28)$$

Hence the dirty image $I_{\rm D}(l,m)$ obtained using Eq. (27) is real.

Noise in Visibility-I

The measured visibilities from the correlator also contain noise whose percentage does not change after calibration. The measured-calibrated visibility $\mathcal{V}_{mc}$ is the sum of noise-less visibility $\mathcal{V}(u,v)$ and noise $\varepsilon(u,v)$ as shown:

$$\mathcal{V}_{\rm mc}(u,v) = \mathcal{V}(u,v) + \epsilon(u,v) \quad \text{... (29)}$$

Let $\varepsilon_{\rm eff}$ represent the effective (rms) noise in the visibility. A fictitious unresolved radio source having a flux density $S_{\rm noise}$ (in watt/m^2/Hz) can be thought to be located at the phase reference point of a noise-free interferometer system which produces this system effective noise output e as shown:

$$\epsilon_{\rm eff} = \sqrt{2}\, S_{\rm noise} \quad \text{... (30)}$$

If ε_i is the complex noise in the $i^{\rm th}$ visibility sample, then it can be expressed as shown below, where $\varepsilon_i^{\rm Re}$ and $\varepsilon_i^{\rm Im}$ respectively represent its real and imaginary parts.

$$\epsilon_i = \epsilon_i^{\rm Re} + j\epsilon_i^{\rm Im} \quad \text{... (31)}$$

Let τ_0 represent the total observation time, and $\tau_{\rm d}$ be the integration time of each visibility data. The number of data points $n_{\rm d}$ on the u-v plane is given as:

$$n_{\rm d} = n_{\rm p}\frac{\tau_0}{\tau_d} \quad \text{... (32)}$$

Here, $n_{\rm p}$ is number of interferometers in the array.

Noise in Visibility-II

The intensity I_0 at the center of the map is given below, where w_i is the weight factor and $\mathcal{V}$ is the noise-free visibility.

$$I_0 = \frac{\sum_{i=1}^{n_d} w_i \left(\mathcal{V} + \epsilon_i^{\mathrm{Re}}\right)}{\sum_{i=1}^{n_d} w_i} \quad \ldots (33)$$

Note that $\varepsilon_i^{\mathrm{Im}} = 0$ at the origin of the u-v plane. The neighboring points possess identical rms noise levels in their real and imaginary parts. For any two different locations on the u-v plane, the noise terms are uncorrelated. Mathematically, $<\varepsilon_i^{\mathrm{Re}}\ \varepsilon_j^{\mathrm{Re}}> = 0$ for $i \neq j$. The variance $\sigma_{\mathrm{m}}^{\ 2}$ of the estimated intensity is:

$$\sigma_{\mathrm{m}}^2 = \left\langle I_0^2 \right\rangle - \left\langle I_0 \right\rangle^2 = \frac{\sum_{i=1}^{n_d} w_i^2 \left\langle \left(\epsilon_i^{\mathrm{Re}}\right)^2 \right\rangle}{\left(\sum_{i=1}^{n_d} w_i\right)^2} \quad \ldots (34)$$

The bracket symbols <> denote averaged over large samples. Let w_{mean} and w_{rms} respectively represent the mean and rms weighting factors. These are related to w_i as:

$$w_{\mathrm{mean}} = \frac{1}{n_d} \sum_{i=1}^{n_d} w_i \quad \ldots (35)$$

$$w_{\mathrm{rms}} = \sqrt{\frac{1}{n_d} \sum_{i=1}^{n_d} w_i^2} \quad \ldots (36)$$

Putting Weight on Visibilities

Practical observations partially fill the u-v plane because (i) visibilities are sampled at discrete points, and (ii) visibility samples are less in number at large projected baselines on the u-v plane. Also the u-v plane is never populated as a square or a rectangle due to Earth rotation. Figure shows a VLA 8 hour observation.

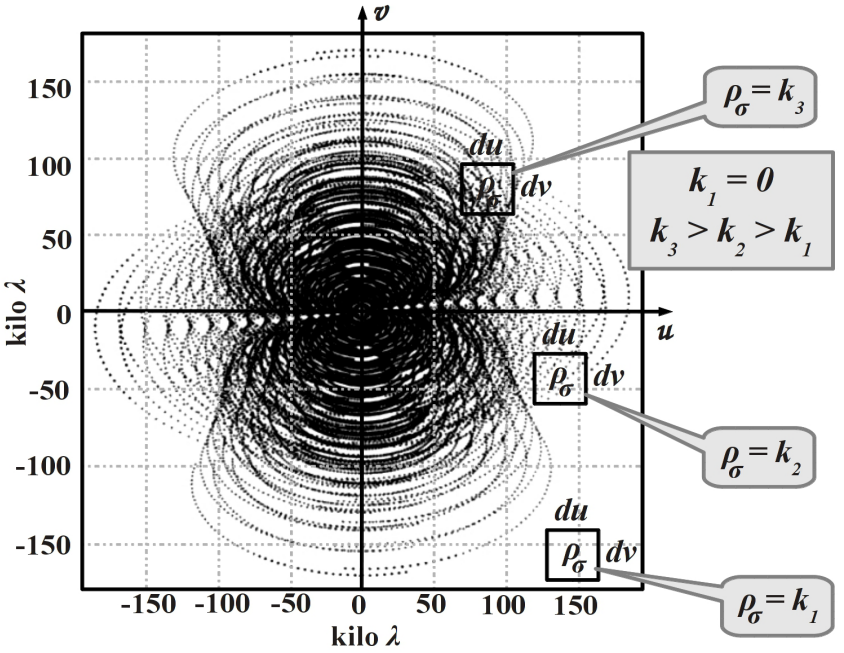

Consider a small rectangular area ($du \times dv$) on the data. Let us define area density ρ_σ which is the number of data points available within the rectangle. In the figure, the area densities k_1, k_2 and k_3 (at three different locations) are not same. Hence, ρ_σ varies from place to place and can be zero at some locations. High data concentrations are seen for shorter u-v spacings. The synthesized beam $P_{\text{syn}}(l,m)$ produces high side-lobe levels due to empty areas resulting in artifacts in the image.

The reciprocal of ρ_σ is sometimes used for weighting the visibilities. Care must be taken that ρ_σ is non-zero by carefully selecting the area of the rectangle.

Imaging with Natural Weights-I

In natural weighting the values of w_i are kept same (usually unity) for all i which means $w_{\text{mean}} = w_{\text{rms}}$. Natural weights give maximum sensitivity at the cost of high side-lobes in the synthesized beam $P_{\text{syn}}(l,m)$ resulting in large artifacts in the dirty image. There exists a relationship between natural weights w_i and effective noise in the visibilities as:

$$w_i = \frac{1}{\sigma_i^2}, \quad \text{where } \sigma = \epsilon_{\text{eff}} \qquad \ldots (37)$$

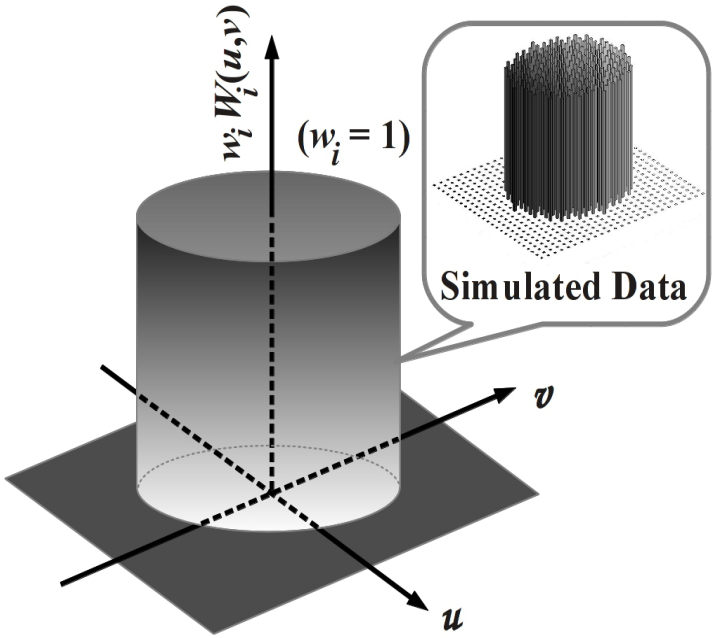

A naturally weighted spatial sensitivity function (simulated by author).

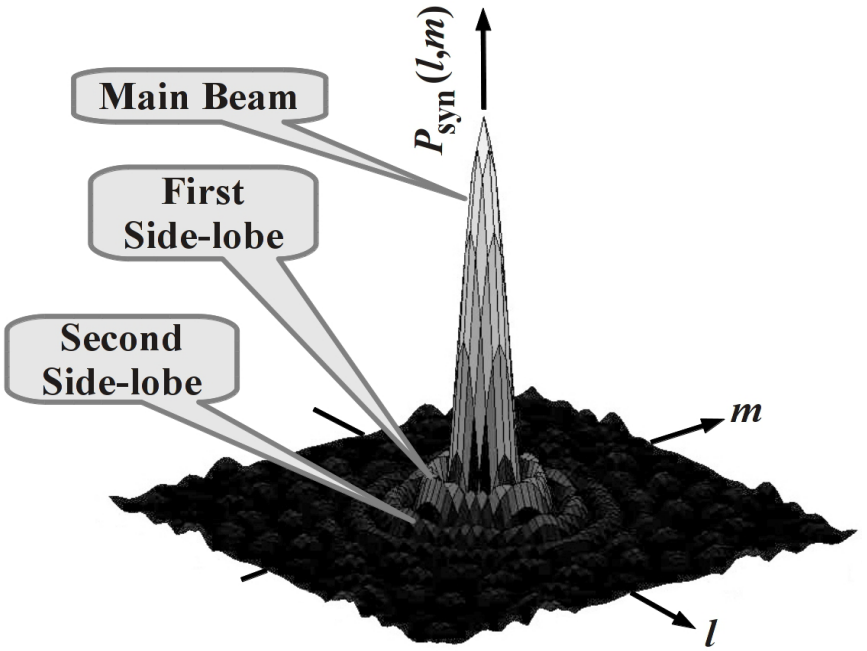

Synthesized beam pattern (simulated by author).

Imaging with Natural Weights-II

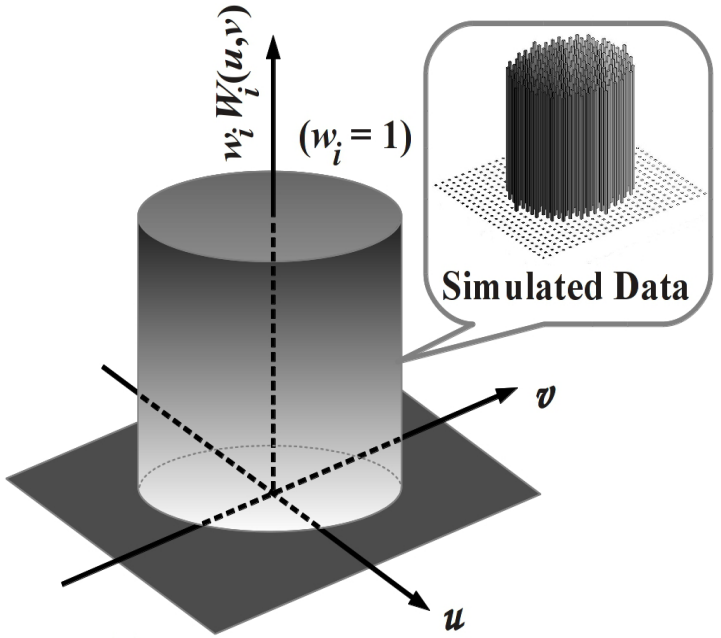

A naturally weighted spatial sensitivity function (simulated by author).

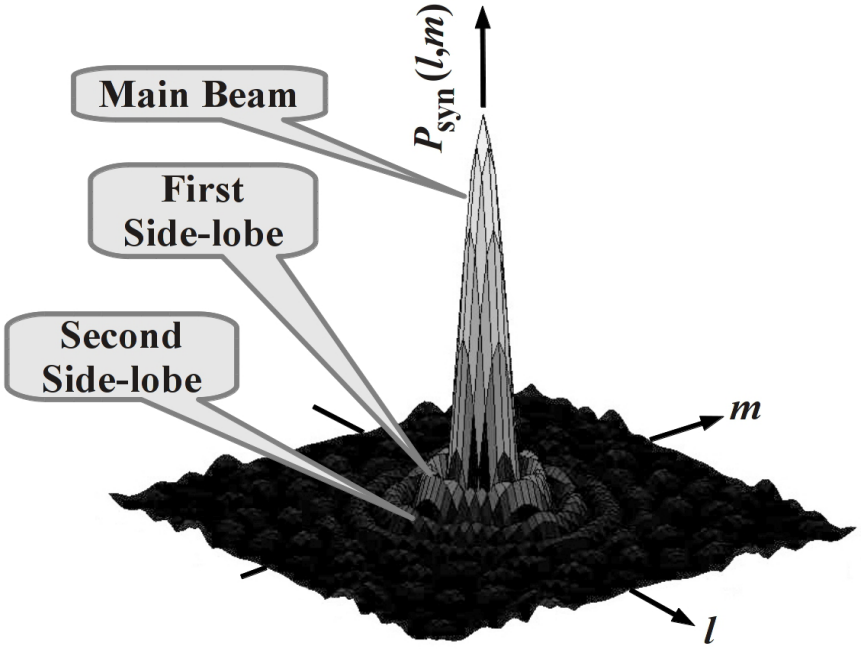

Synthesized beam pattern (simulated by author).

Note that the side-lobes are significantly strong to produce artifacts in the image. The main reason for side-lobes is the step-fall of spatial sensitivity function beyond a certain radius. In actual data, there exists a hole in the middle portion of the cylinder due to absence of data below minimum baseline distances. Also, the data density falls with increasing baseline length and abruptly stops above the maximum baseline length. The shape of the data area need not be circular as shown. All of these contribute to form different side-lobe structures.

Imaging with Uniform Weights-I

As shown, the visibility population on u-v plane is not uniform. Since the visibilities are discrete, many places on the u-v plane are empty. As the projected baselines become smaller, the discrete data becomes denser on the u-v plane. Hence the SNR is not uniform across the u-v plane. To obtain an uniform SNR we first evaluate the area density $\rho_{\sigma i}$ as a function of u,v. A least square fitting may be used for a general case. After evaluating the function $\rho_{\sigma i} = \rho_{\sigma}(u_i, v_i)$, weights are applied as shown below, where k_0 is a constant (usually unity).

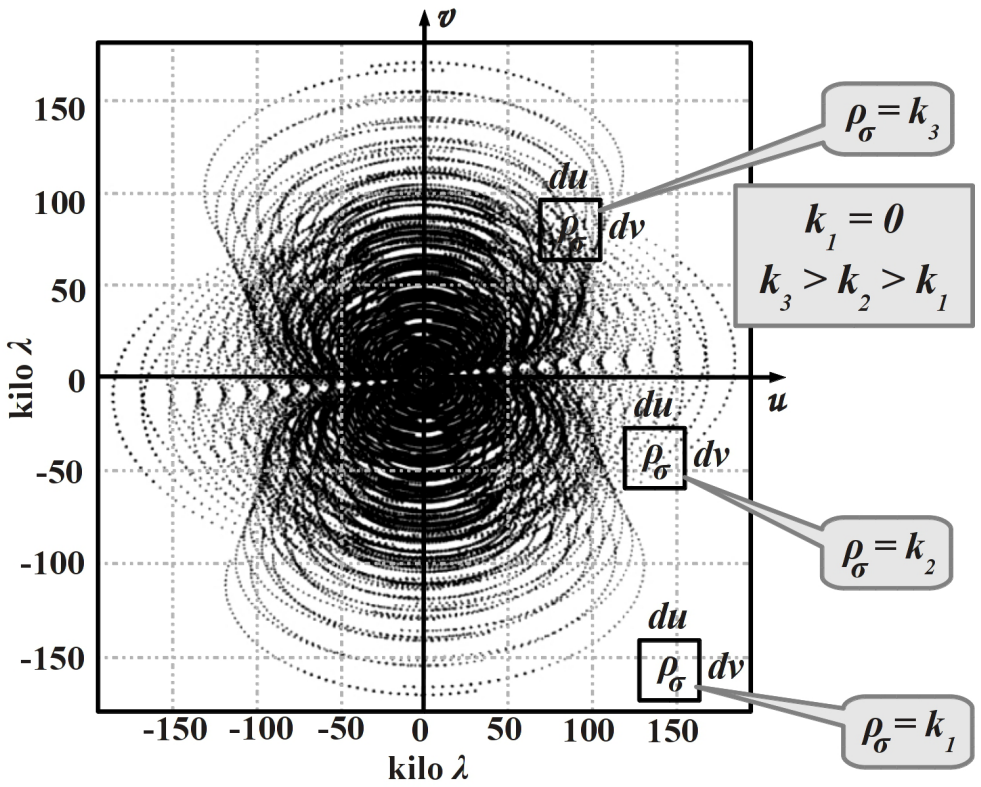

$$w_i = \frac{k_0}{\rho_{\sigma i}}, \quad 1 \le i \le n_{\mathrm{d}} \qquad \ldots (38)$$

When the area density function $\rho_{\sigma i}$ is uniform across the u-v plane, the weighting turns out to be a natural.

Imaging with Uniform Weights-II

A East-West array having ten unique baselines (multiples of the smallest baseline) observs a source at CNP for 12 hours. The simulated spatial sensitivity functions and beam shapes for natural and uniform weights are shown. Visibilities discretely appear along circles over the u-v plane. The radii of these circles are multiples of the smallest baseline.

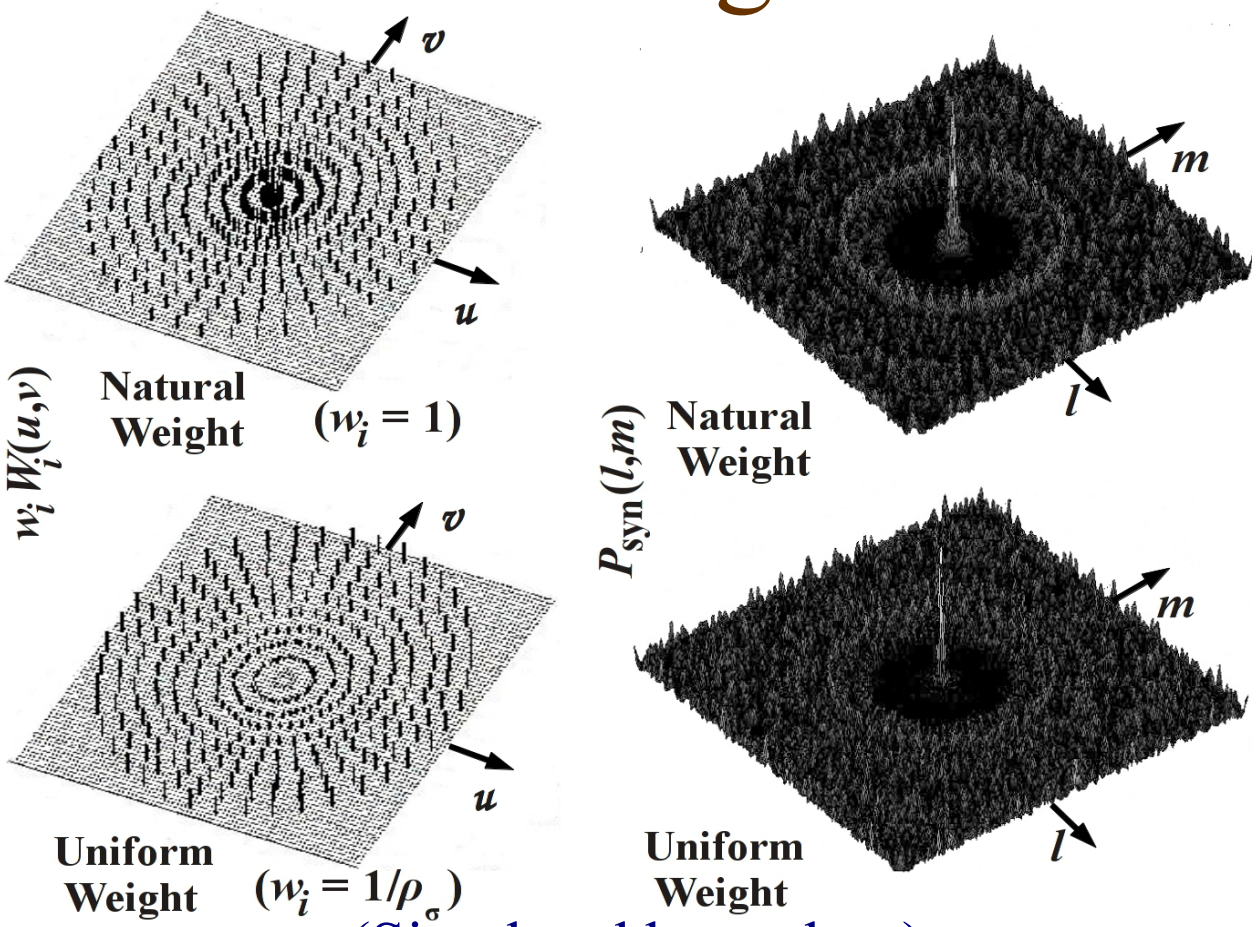

(Simulated by author.)

The naturally weighted spatial sensitivity function appear as cylindrical fences of different radii but equal heights. Since the number of data points on each circle are same, ρ_σ is minimum on the largest circle and maximum on the smallest circle. Hence, ρ_σ on the circles are inversely proportional to their radii. To achieve an uniform SNR, divide the upper function by ρ_σ. The result is the uniformly weighted function shown.

Imaging with Uniform Weights-III

The main beam resulting from uniform weights is relatively narrower. The neighboring side-lobes are also relatively smaller than those produced by natural weights. The distant side-lobes however increase with uniform weights. These effects are visible on the images (see right).

Rectangular data set is needed for FFT. Since the u-v data set are usually composed of circles and ellipses, a rectangular data set must be generated by padding zeros outside the area of the actual data as shown in last slide.

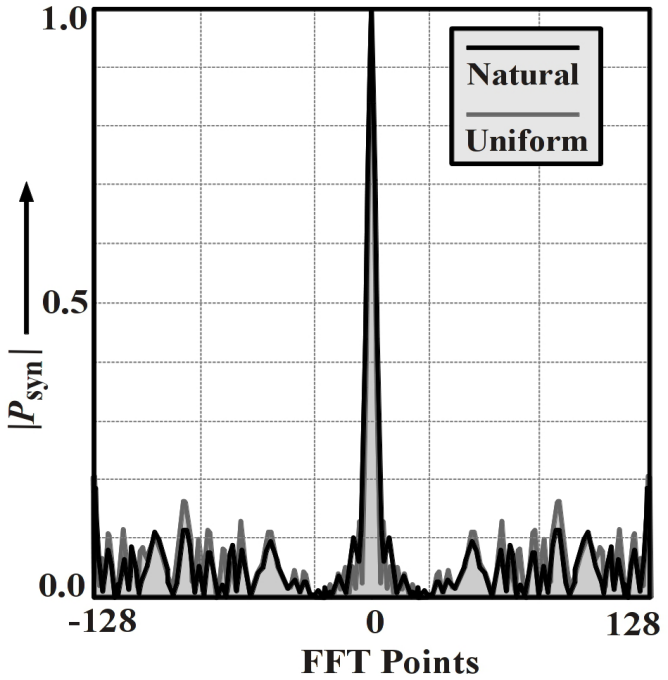

(Simulated by author.)

Images formed using:
(a) Natural weights.
(b) Uniform weights.

Note: Uniform weights gives higher resolution at the cost of reduced sensitivity.

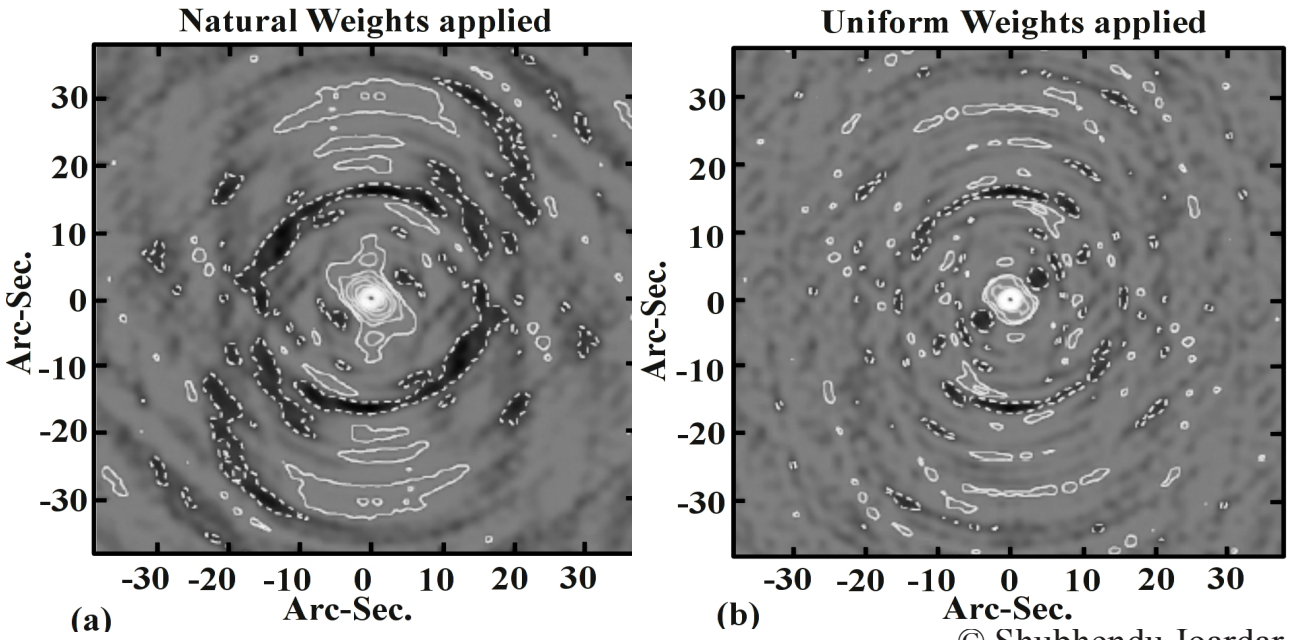

Imaging with Tapered Weights-I

Though uniform weights are preferable to natural weights, still the magnitude of side lobes remain quite high close to the main beam, which reduces image details having low intensity profile. To reduce these side-lobes a tapered weightage w_i of the form shown below (Gaussian tapering) may be used with $W(u,v)$, where ζ represents the tapering parameter, i is the sample number, and n_{d} represents the total number of discrete visibilities (see Eq. (32)). Since u and v axes are in number of wavelengths, ζ also uses the same dimension.

$$w_i = \exp\left[-\frac{u_i^2 + v_i^2}{\zeta_i^2}\right], \text{ where, } i = 1, 2, \ldots n_{\mathrm{d}} \quad \ldots (39)$$

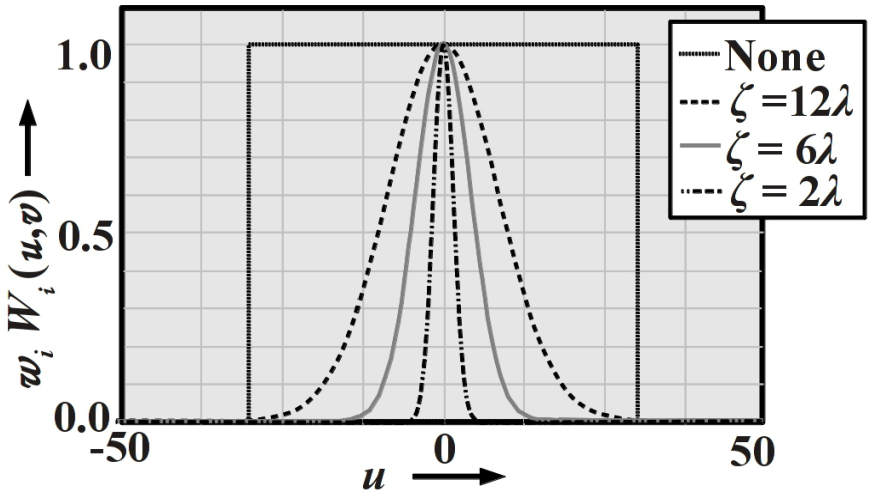

Tapering applied to $W(u,v)$ by modifying w_i (simulated by author).

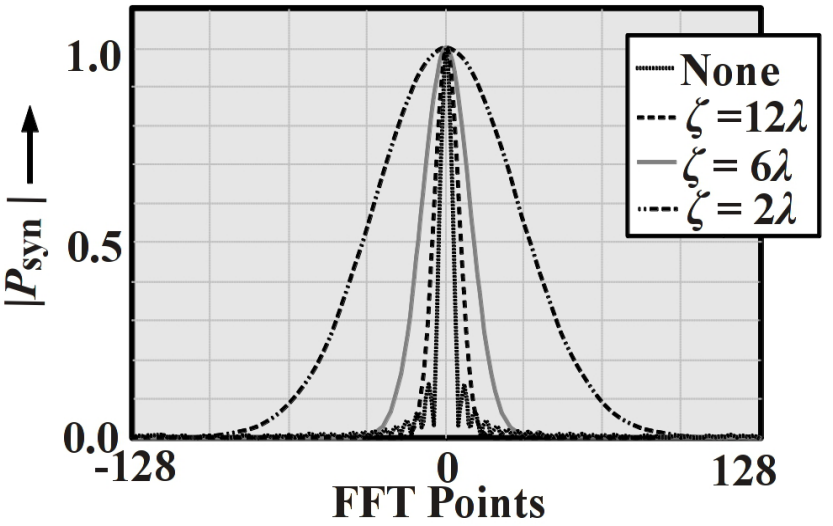

Magnitude of resulting synthesized beam $|P_{\mathrm{syn}}|$ (simulated by author).

Imaging with Tapered Weights-II

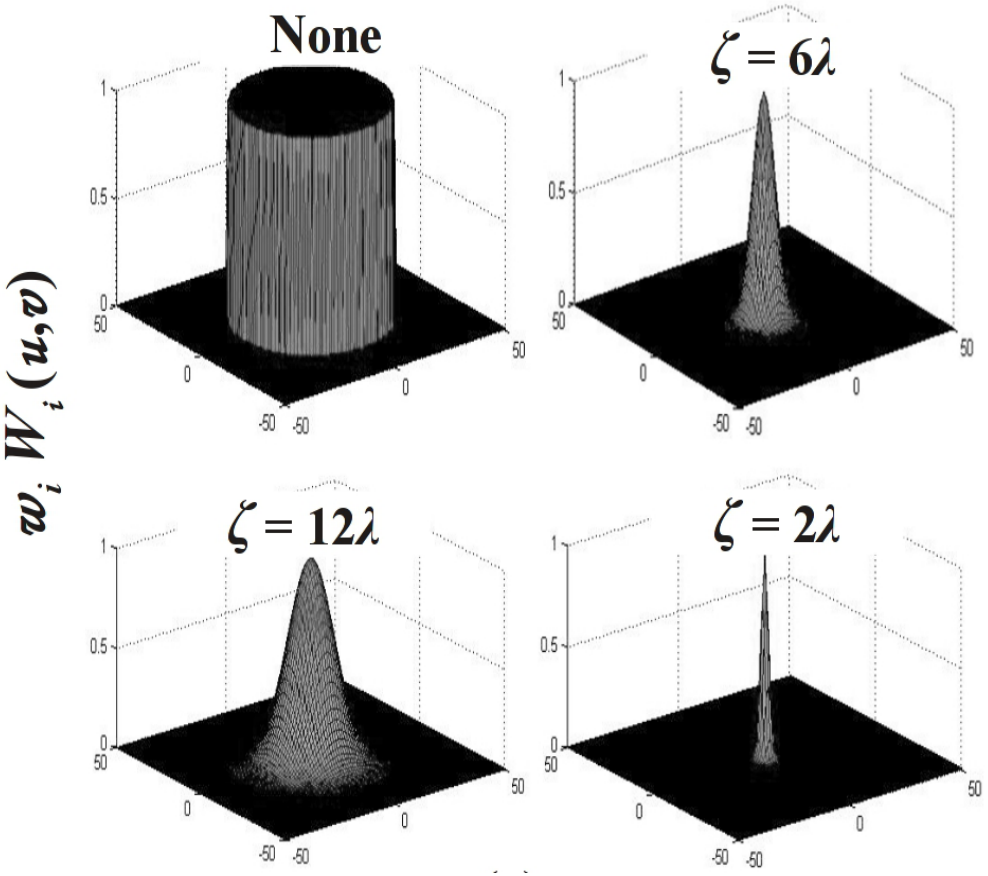

Three dimensional view of tapered $W(u,v)$ (simulated by author).

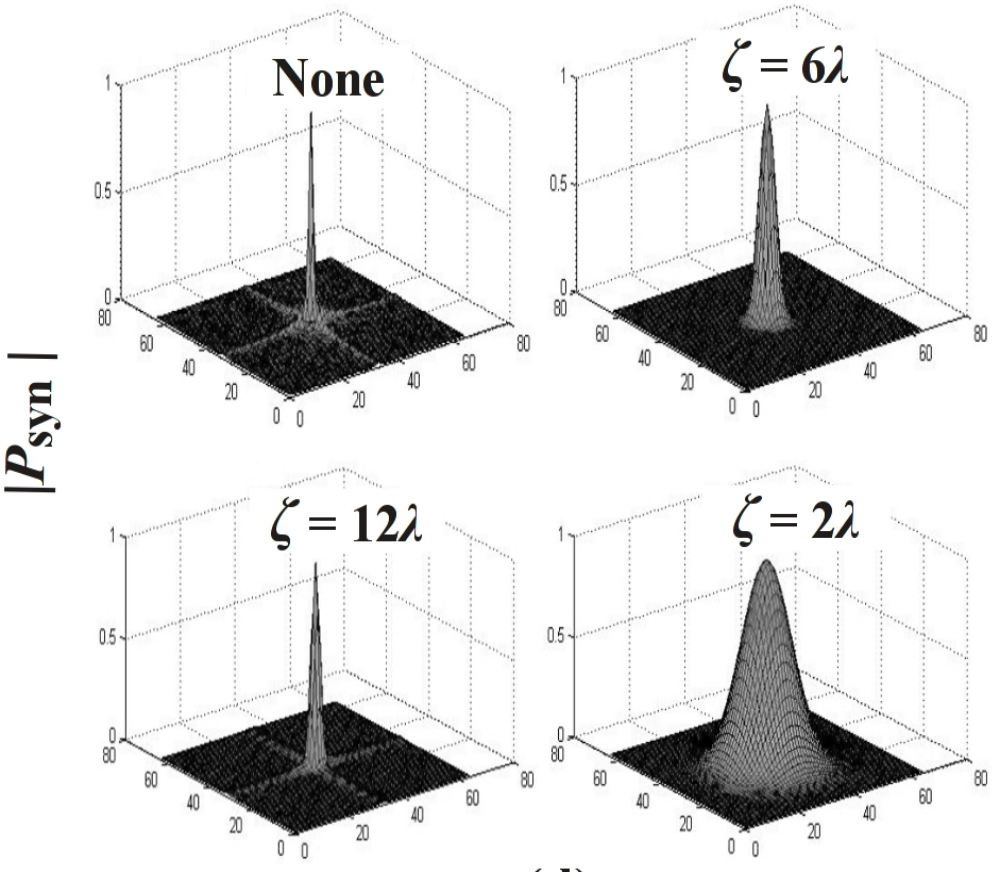

Three dimensional plot of $|P_{syn}|$ (Simulated by author).

Note: The side-lobes reduce as tapering increases (decreasing ζ), but at an expense of increased main beam-width.

Imaging with Tapered Weights-III

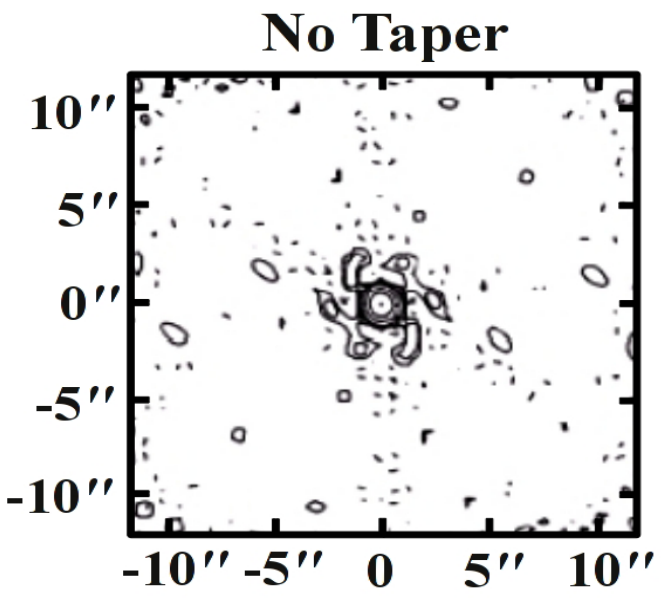

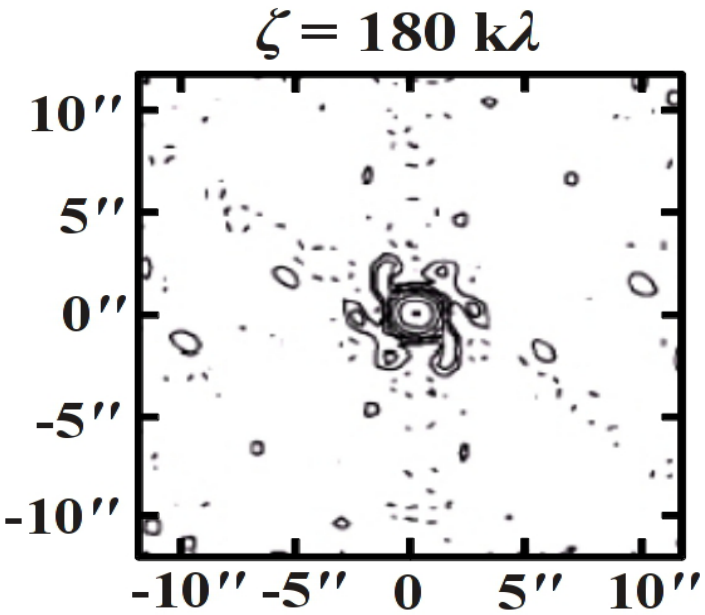

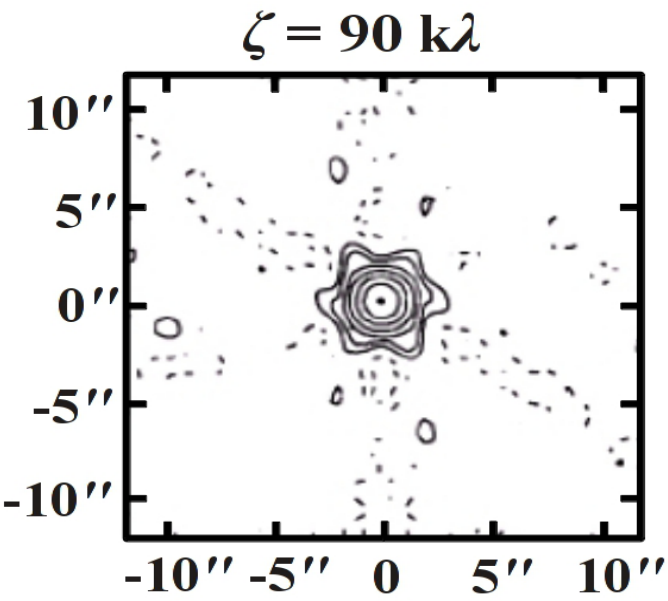

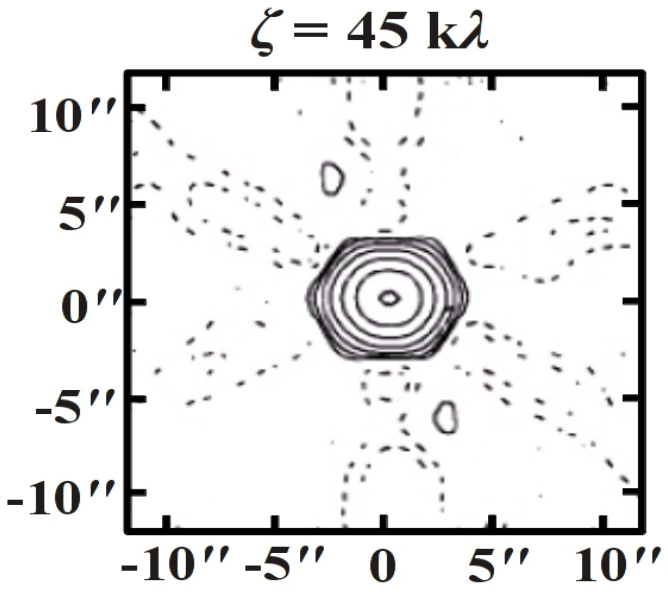

Gaussian taperings are most commonly used for its better ability to reduce neighboring side-lobes. Tapering functions like cosine may be used with some compromise between main beam-width and side-lobes.

Imaging with Robust Weights-I

Another weighting function known as ***robust weighting*** is gaining popularity. It is a compromise between uniform and natural weights based on the local SNR of the visibilities in *u-v* plane. When area density ρ_σ is less than a chosen threshold level, natural weights are used, otherwise uniform weights are applied. The algorithm is:

$$w_i = \frac{1}{S^2 + \sigma_i^2}, \quad \text{where } S = k_1 \times 10^{-R}, \quad \text{and } \sigma = \epsilon_{eff} \qquad \ldots (40)$$

Here, the filter S is controlled by the robust parameter R, and σ represents effective (rms) noise as obtained in Eq. (30). The constant k_1 may be around 5 or so.

By a proper selection of the robust parameter R, it may be possible to apply natural weights when the area density ρ_σ is small, and uniform weights otherwise.

Imaging with Robust Weights-II

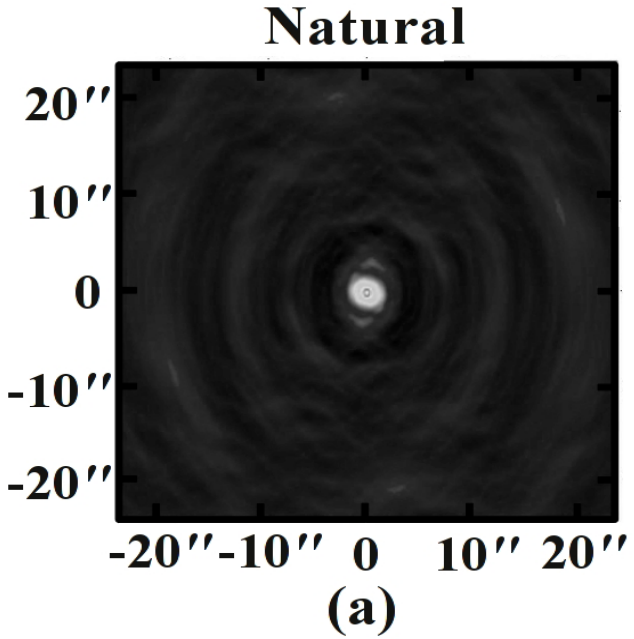

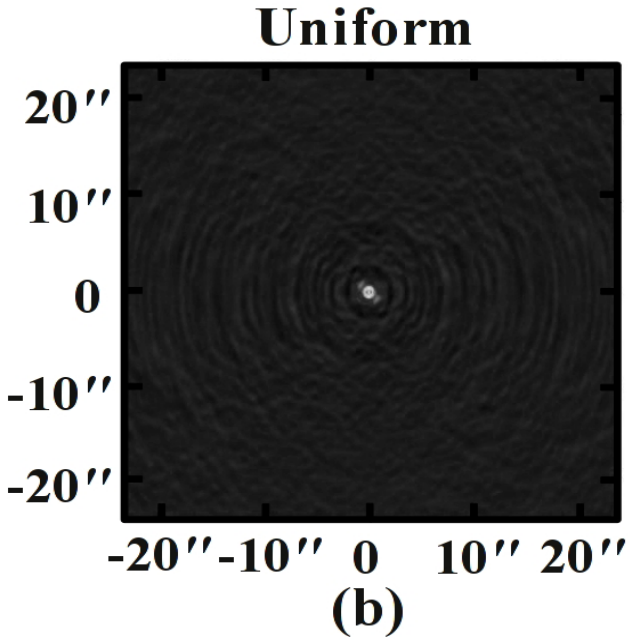

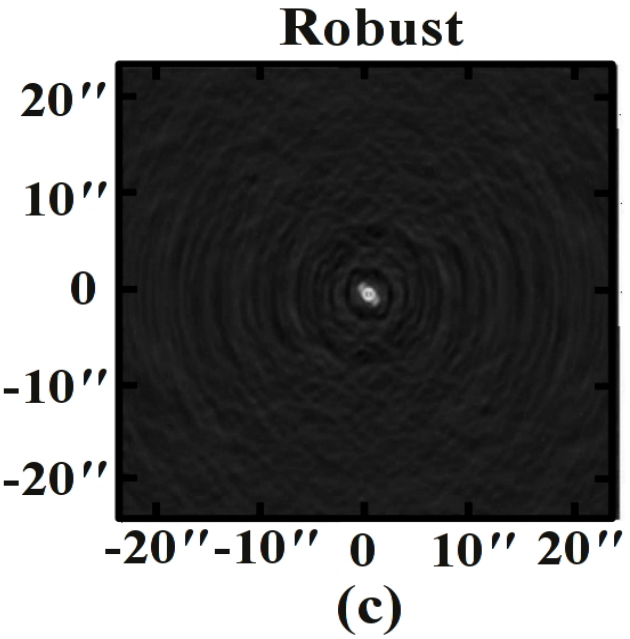

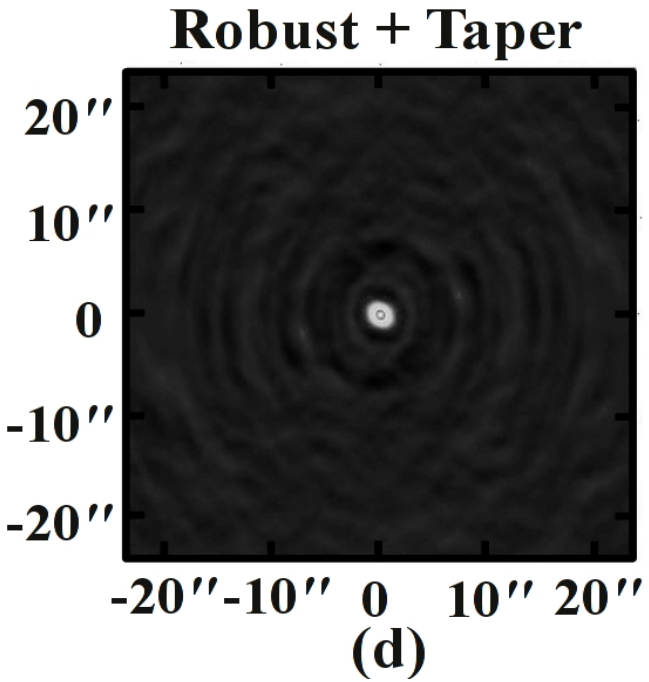

(a) With natural weights, HPBW is maximum and the noise variance is minimum. Side-lobes are prominent especially near the main beam. (b) With uniform weights, beam-width is minimum but noise variance is maximum. (c) With robust weights, beam-width slightly increases but noise variance is relatively small. (d) Applying taper on robust weights, beam-width is brought back to natural, but noise variance has increased. The nearby side-lobes however have been reduced.

Gridding Visibilities for FFT-I

Spacing between the visibility data samples on the u-v plane varies with the changing shape of the projected baselines due to Earth rotation. Hence, the spacings are not equal as shown.

For performing FFT, the sampled visibility data points should be equally spaced along both u and v coordinates. Hence, the non-uniformly spaced visibilities $\mathcal{V}(u_i,v_i)$ are convolved with a continuous function and the resulting continuous function is again sampled with equal spacings to fill the u-v plane. Generally, the sampling is done by a comb function.

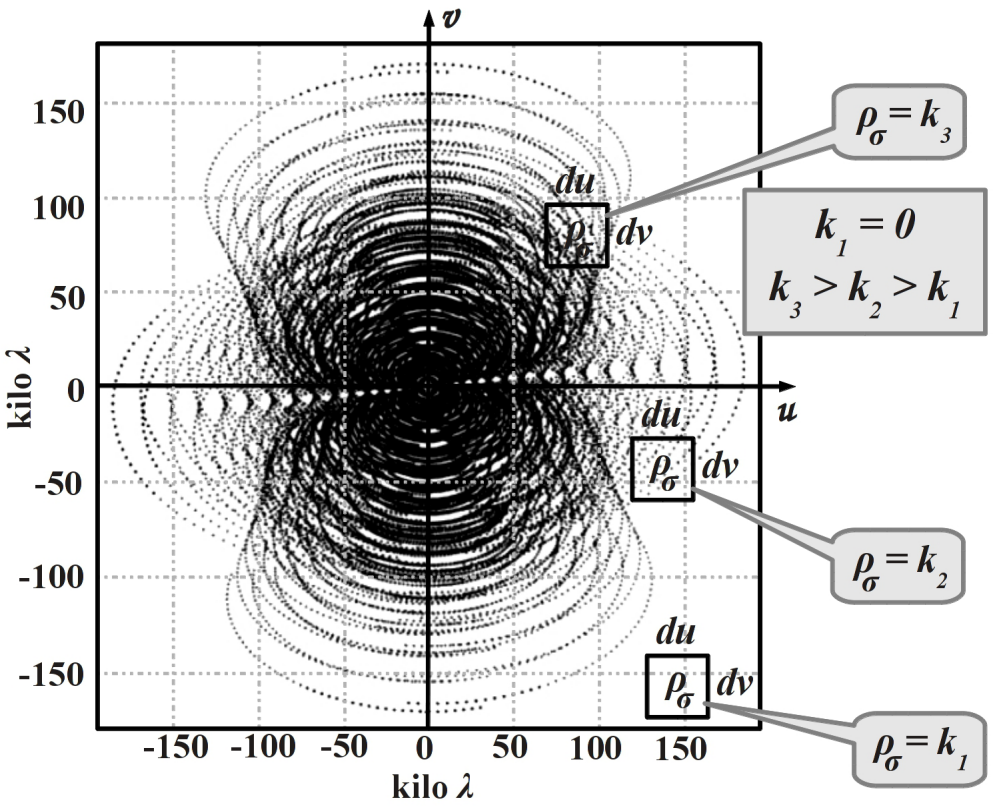

Note: This interpolation process is only an approximation but unavoidable.

Gridding Visibilities for FFT-II

$f_1(x')$ - convolving function.

$f_2(x')$ - amplitudes of data points as function of some variable x'.

$f_3(x')$ - convolved product of f_1 and f_2.

$f_4(x')$ - another sampling function.

$f_5(x')$ - gridded result of sampling f_3 at equal intervals of x' by $f_4(x')$.

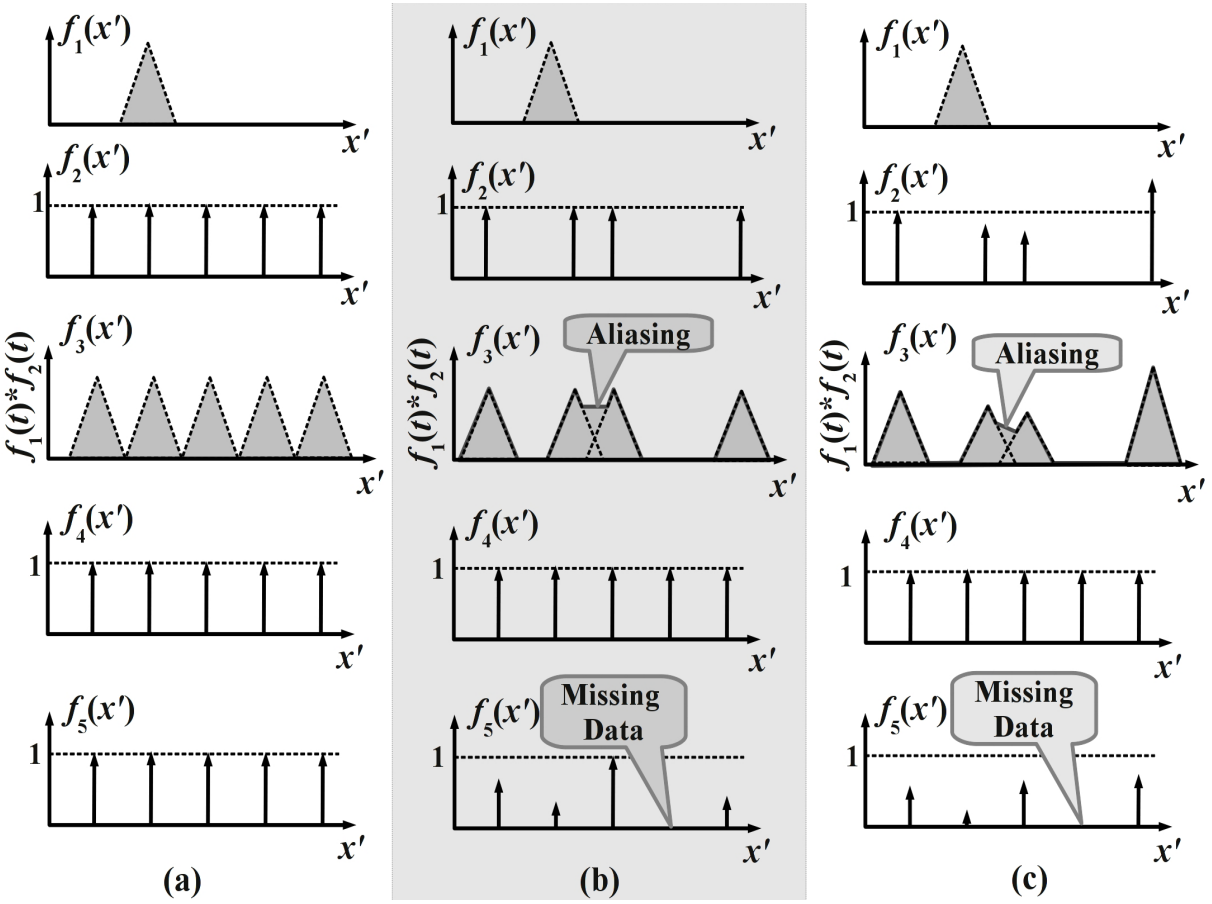

(a) $f_2(x')$ - uniform magnitude, equally spaced. Resulting $f_5(x')$ resembles with $f_2(x')$. (b) $f_2(x')$ - uniform magnitude, not equally spaced. Due to aliasing, $f_5(x')$ differs from $f_2(x')$. Amplitudes of $f_5(x')$ at grid points are not uniform and some data points are missing. (c) $f_2(x')$ - non-uniform magnitude, not equally spaced. Here also, $f_5(x')$ differs from $f_2(x')$. Amplitudes of $f_5(x')$ are not uniform and some data points are missing.

Gridding Visibilities for FFT-III

Difficulties experienced in one dimensional gridding also exist for two dimensions. Let $C(u,v)$ represent the convolving function. For simplicity, the most basic model (without weight factor) of measured-calibrated visibility $\mathcal{V}_{mc}(u,v)$ is used. It is shown below:

$$\mathcal{V}_{mc}(u,v) = \mathcal{V}(u,v)\, W(u,v) \qquad \ldots (41)$$

Note that Eq. (41) is a product of true visibility $\mathcal{V}(u,v)$ and spatial sensitivity function $W(u,v)$ as shown.

With analogy to f_1 from previous figure (previous slide), the convolving function is given as:

$$f_1(u,v) = C(u,v) \qquad \ldots (42)$$

Similarly, $\mathcal{V}_{mc}$ is analogous to f_2 and can be expressed as:

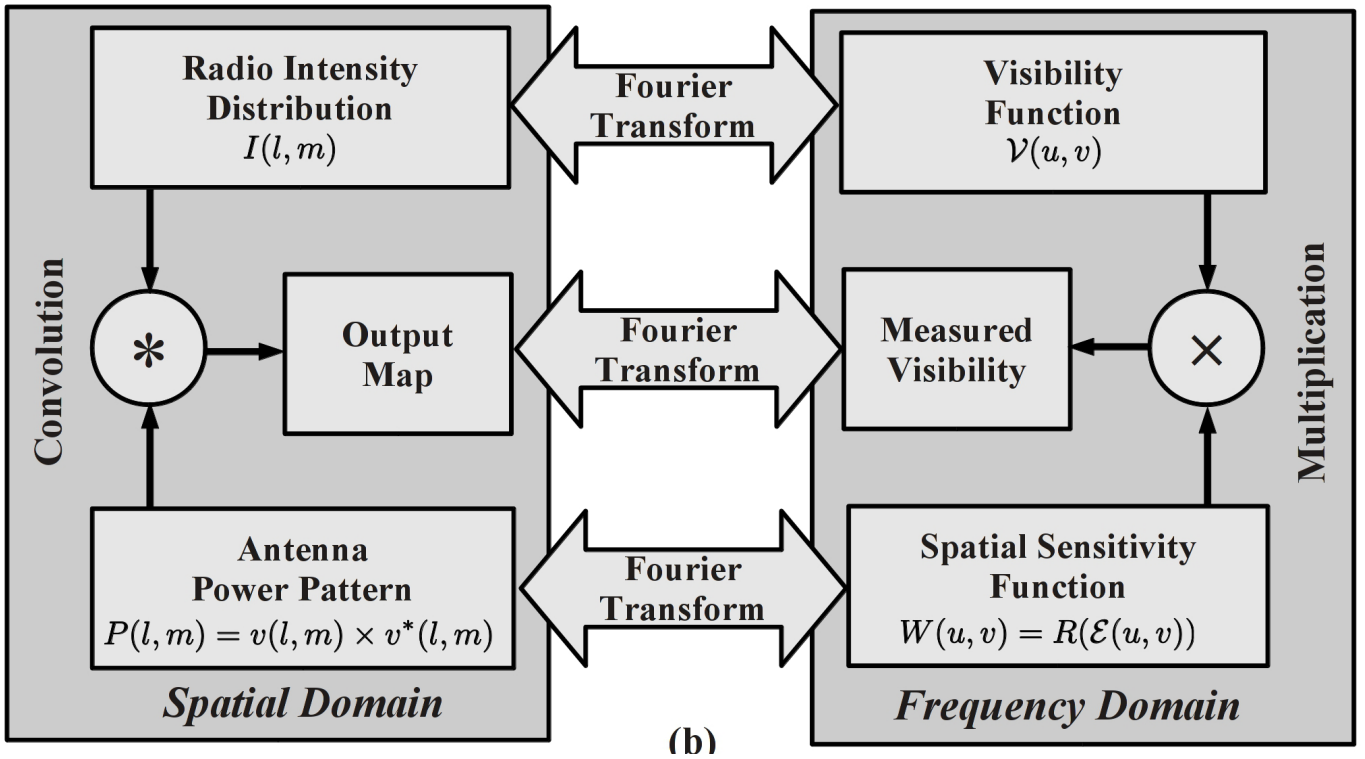

$$f_2(u,v) = \mathcal{V}_{mc}(u,v) = \mathcal{V}(u,v)\, W(u,v) \qquad \ldots (43)$$

Gridding Visibilities for FFT-III

From previous slide ...

$$\mathcal{V}_{\rm mc}(u,v) = \mathcal{V}(u,v)\, W(u,v) \quad \text{... (41)}$$

$$f_1(u,v) = C(u,v) \quad \text{... (42)}$$

$$f_2(u,v) = \mathcal{V}_{\rm mc}(u,v) = \mathcal{V}(u,v)\, W(u,v) \quad \text{... (43)}$$

And finally, using the same analogy we have:

$$f_3(u,v) = C(u,v) * [\mathcal{V}(u,v)\, W(u,v)] \quad \text{... (44)}$$

Let Δu and Δv respectively represent the minimum (gridding) distances along u and v. A comb function can be used to represent $f_4(u,v)$ as:

$$f_4(u,v) = \text{comb}\,(\Delta u,\ \Delta v) = \sum_{p=-\infty}^{\infty} \sum_{q=-\infty}^{\infty} \delta_{\rm II}\,(u - p\,\Delta u,\ \ v - q\,\Delta v) \quad \text{... (45)}$$

Here p and q are integers ranging from $-\infty$ to $+\infty$. Basically, $\delta_{\rm II}(u\text{-}p\Delta u, v\text{-}q\Delta v)$ is a two dimensional delta function shifted by $p\Delta u$ along u-axis and by $q\Delta v$ along v-axis. It looks like as a bed of nails of unit height having separations of Δu and Δv respectively along u and v axes.

Sampling using the comb function results $f_5(u,v)$ as:

$$f_5(u,v) = \text{comb}\,(\Delta u,\ \Delta v)\,[C(u,v) * \{\mathcal{V}(u,v)\, W(u,v)\}] = \mathcal{V}_{\rm grd}(u,v) \quad \text{... (46)}$$

The above is same as the gridded visibilities $\mathcal{V}_{\rm grd}(u,v)$.

Effect of Convolution Gridding on Image-I

Let $I_{\rm grd}(l,m)$ represent the image resulting from the gridded visibilities. It is obtained from the Fourier transform of $\mathcal{V}_{\rm grd}(u,v)$ as:

$$I_{\rm grd}(l,m) = \overline{\mathcal{V}}_{\rm grd}(l,m) = \left[\frac{\mathrm{comb}\,(\Delta l,\ \Delta m)}{\Delta u\,\Delta v}\right] * \left[\overline{C}(l,m)\left\{\overline{\mathcal{V}}(l,m) * \overline{W}(l,m)\right\}\right] \quad \ldots (47)$$

Here, $\overline{\mathcal{V}}_{\rm grd}$, $\overline{\mathcal{V}}$, $\overline{W}$ respectively represent the Fourier transforms of $\mathcal{V}_{\rm grd}$, $\mathcal{V}$ and W.

The details of the function comb(Δl,Δm) are given below, where p' and q' represent integers ranging from -∞ to +∞.

$$\mathrm{comb}\,(\Delta l,\ \Delta m) = \left\{ \begin{array}{c} \sum_{p'=-\infty}^{\infty} \sum_{q'=-\infty}^{\infty} \delta_{\rm II}\,(u - p'\,\Delta l,\ \ v - q'\,\Delta m) \\ \text{where, } \Delta l = \frac{1}{\Delta u},\ \Delta m = \frac{1}{\Delta v} \end{array} \right\} \quad \ldots (48)$$

Note that the intensity distribution of the sky is $I(l,m) = \overline{\mathcal{V}}(l,m)$. Rearranging Eq. (47) we obtain $I_{\rm grd}(l,m)$ as:

$$I_{\rm grd}(l,m) = \left[\frac{\mathrm{comb}\,(\Delta l,\ \Delta m)}{\Delta u\,\Delta v}\right] * \left[\overline{C}(l,m)\left\{I(l,m) * \overline{W}(l,m)\right\}\right] \quad \ldots (49)$$

Effect of Convolution Gridding on Image-II

Most of the image information is hidden in the shape of $I(l,m) * \overline{W}(l,m)$, which is a convolution between spatial intensity distribution of the sky $I(l,m)$ and beam pattern $\overline{W}(l,m)$.

More resemblance between shapes of $I(l,m) * \overline{W}(l,m)$ and $\overline{C}(l,m)\{I(l,m) * \overline{W}(l,m)\}$ produces less distortion in the image $I_{grd}(l,m)$. Hence $\overline{C}(l,m)$ should have a flat shape so that it uniformly scales $I(l,m) * \overline{W}(l,m)$ without changing its shape.

As the function $\overline{C}(l,m)\{I(l,m) * \overline{W}(l,m)\}$ grows wider along l and m axes, the aliasing chances increase during convolution with comb$(\Delta l, \Delta m)$. Hence, ideally $\overline{C}(l,m)$ should have a rectangular shape to restrict the widths of $I(l,m) * \overline{W}(l,m)$.

Gridding Functions

If the function $C(u,v)$ can be generated from two independent functions $C_1(u)$ and $C_2(v)$ as shown below, then they become separable and can be applied with more ease.

$$C(u,v) = C_1(u)\, C_2(v) \quad \text{... (50)}$$

Some one dimensional convolving functions useable with above equation are described next. These are:

(*i*) Rectangular.
(*ii*) Gaussian.
(*iii*) Gaussian-Sinc.
(*iv*) Spheriodal functions.

Gridding Fncs.: Rectangular Function

A rectangular function is described below:

$$C_{\text{Rect}}(x) = \begin{cases} 1, & |x| \le \frac{1}{2} \\ 0, & |x| > \frac{1}{2} \end{cases} \quad w_i \qquad \ldots (51)$$

Using this we may define $C_1(u)$ as:

$$C_1(u) = \frac{1}{\Delta u} C_{\text{Rect}}(u) \qquad \ldots (52)$$

We may also define $C_2(v)$ in a similar way by replacing u with v.

The response of this function (Eq. (52)) is a sinc function as given below, which is obtained by taking its Fourier transformation.

$$\overline{C}_1(l) = \frac{\sin(\pi \Delta u\, l)}{\pi \Delta u\, l} = \text{sinc}(\pi \Delta u\, l) \qquad \ldots (53)$$

It extends to infinity resulting in significant amount of aliasing. A Gaussian function may be a better choice.

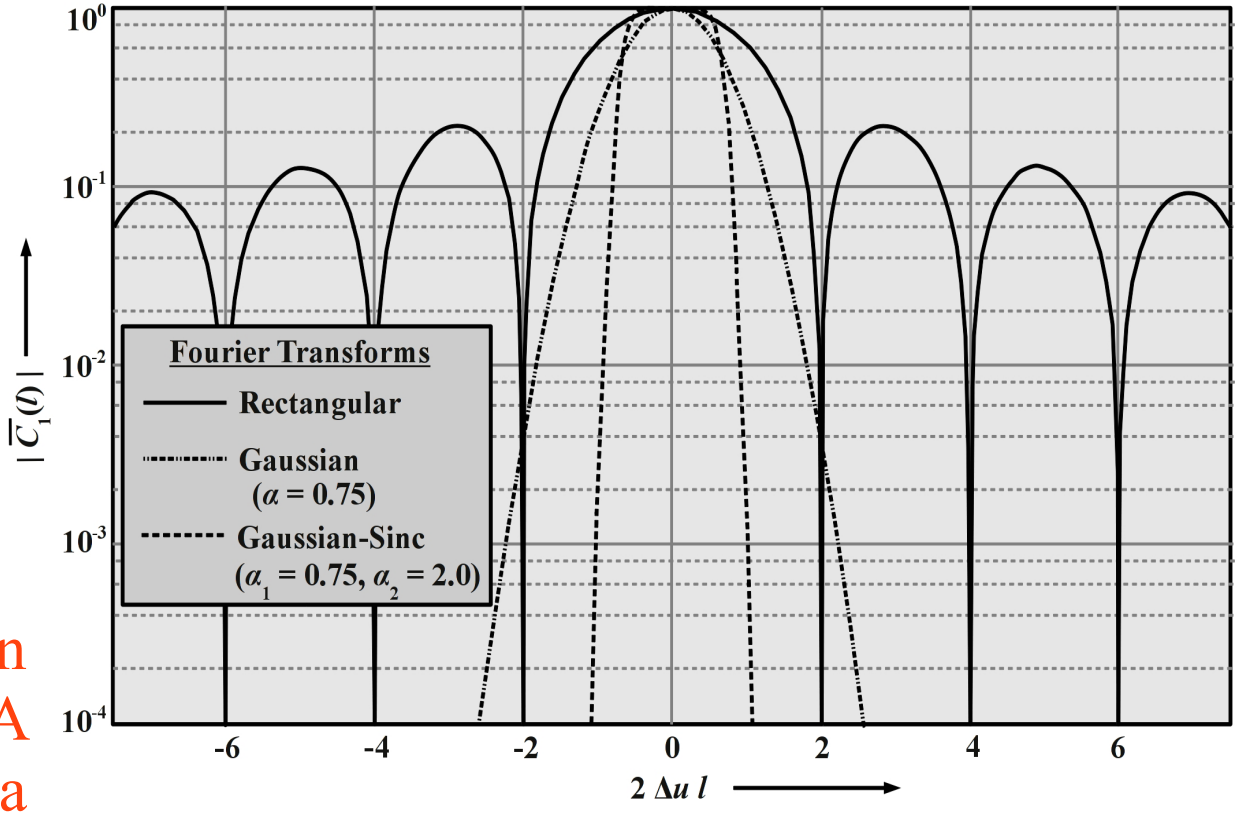

Gridding Fncs.: Gaussian Function

A Gaussian function is shown below:

$$C_1(u) = C_{\text{Gauss}}(u) = \frac{1}{\alpha\,\Delta u\,\sqrt{\pi}} \exp\left[-\left(\frac{u}{\alpha \Delta u}\right)^2\right] \quad \text{... (54)}$$

$$\overline{C}_1(l) = \exp\left[-(\pi\alpha\Delta u\, l)^2\right] \quad \text{... (55)}$$

A desired width from the function $C_1(u)$ can be obtained by varying the value of α. Small values of α makes $C_1(u)$ appear narrow. Hence, contributions come from only those data which are close to the grid points.

When α is large, $\overline{C}_1(l)$ can severely taper the map. Hence the choice of is in between. Generally, α is given a value close to 0.75. Magnitude variations of $\overline{C}_1(l)$ for $\alpha = 0.75$ is shown using dashed-dotted lines in the last figure.

Although a Gaussian function performs better than a rectangular function, it is not ideal for producing rectangular shapes in the spatial (l,m) domain. A further improved function may be a product of Gaussian and sinc functions. It is described next.

Gridding Fncs.: Gaussian-Sinc Function

A Gaussian-sinc function is expressed as:

$$C_1(u) = C_{\text{GaussSinc}}(u) = \frac{\text{sinc}\left[\frac{\pi u}{\alpha_1 \Delta u}\right] \exp\left[-\left(\frac{u}{\alpha_2 \Delta u}\right)^2\right]}{\alpha_1 \Delta u} \quad \ldots (56)$$

Its Fourier transform is given as:

$$\overline{C}_1(l) = [C_{\text{Rect}}(\alpha_1 \Delta u)] * \left[\left(\sqrt{\pi}\alpha_2 \Delta u\right) \exp\left\{-\left(\pi \alpha_2 \Delta u\, l\right)^2\right\}\right] \quad \ldots (57)$$

The above is a convolution between the Fourier transforms of sinc and Gaussian functions. It may be seen as a convolution of a rectangular function with a Gaussian function in the spatial (l,m) domain.

With $\alpha_1 = 0.75$ and $\alpha_2 = 2.0$, the magnitude of $\overline{C}_1(l)$ is plotted with a dashed line in last figure. Note the central region around the peak. It is flat. The fall is sharp which resembles to a distorted rectangular function in the spatial domain.

Convolving functions discussed so far may not be optimal choices for gridding. Based on the desired gridding properties, a completely different approach may be taken. The major requirements are: (i) $\overline{C}_1(l)$ must sharply fall off, and (ii) it must be flat around the center. A class of functions called spheroidal functions may be a better choice. These are described next.

Gridding Fncs.: Spheriodal Functions-I

These are solutions to Laplace equation. These are found by expressing the equation in spheroidal coordinates and then applying the technique of separation of variables.

The utility of a convolving function is judged from the placement and magnitude of the aliasing side-lobes after the image is corrected for roll off at the edges. Let η_{sup} represent a measure of effectiveness of suppressing aliases. It may be described as:

$$\eta_{sup} = \frac{\int\int_{\text{map}} \left[\overline{C}(l,m)\right]^2 dl\, dm}{\int_{\infty}^{\infty}\int_{\infty}^{\infty} \left[\overline{C}(l,m)\right]^2 dl\, dm}, \text{ where } \eta_{sup} \leq 1 \quad \ldots (58)$$

Note: Same expression for integration are used in both numerator and denominator, but with different limits. Within the map, the numerator gives the total sum of $\left[\overline{C}(l,m)\right]^2$. The denominator gives the same over the whole (within and outside the map). Hence, $\overline{C}(l,m)$ should be such that sum is nearly unity. Instead of prolate spheroidal functions which are difficult to calculate, a simple approximation using a Kaiser-Bessel window function as:

$$C_1(u) = \frac{1}{L} I_0 \left[B\sqrt{1 - \left(\frac{2u}{L}\right)^2} \right], \; u < \frac{L}{2} \quad \ldots (59)$$

Here, I_0 represents a zero order modified Bessel function of the first kind. Constants B and L determine window characteristics in inverse transform.

Gridding Fncs.: Spheriodal Functions-II

Constants B and L determine window characteristics in inverse transform as:

$$\overline{C}_1(l) = \frac{\sin\left(\sqrt{\pi^2 L^2 l^2 - B^2}\right)}{\sqrt{\pi^2 L^2 l^2 - B^2}} \qquad \ldots (60)$$

In two dimensions, the function is obtained as $C(u,v) = C_1(u)C_2(v)$. The values of B are chosen using:

$$\left.\begin{aligned} B_l &= \pi L_l l_1 \\ B_m &= \pi L_m m_1 \end{aligned}\right\} \qquad \ldots (61)$$

The first nulls of $\overline{C}(l,m)$ occur at $|l| = \pm(l_1^2 + 1/L^2)^{1/2}$ and $|m| = \pm(m_1^2 + 1/L^2)^{1/2}$.

The inverse operation using discrete Fourier transform will be performed on a set of discrete points in such a way that the points $|l| = l_1$ and $|m| = m_1$ become the folding points in the transform. To get this, $l_1 = 1/(2u_0)$ and $m_1 = 1/(2v_0)$. By making $\overline{C}_1(l)$ and $\overline{C}_2(m)$ to cover the L_l, L_m points in the Fourier domain, we get the values of B_l and B_m as shown below. The grid interval is kept unity.

$$\left.\begin{aligned} B_l &= \pi L_l/2 \\ B_m &= \pi L_m/2 \end{aligned}\right\} \qquad \ldots (62)$$

Gridding Fncs.: Spheriodal Functions-III

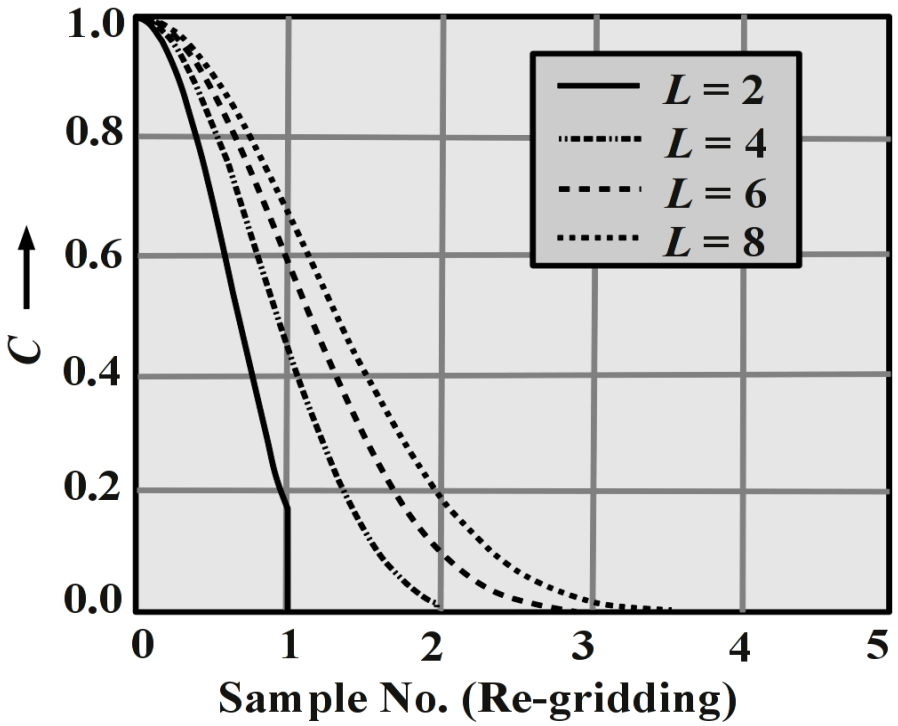

Kaiser-Bessel convolving function with different extents L .

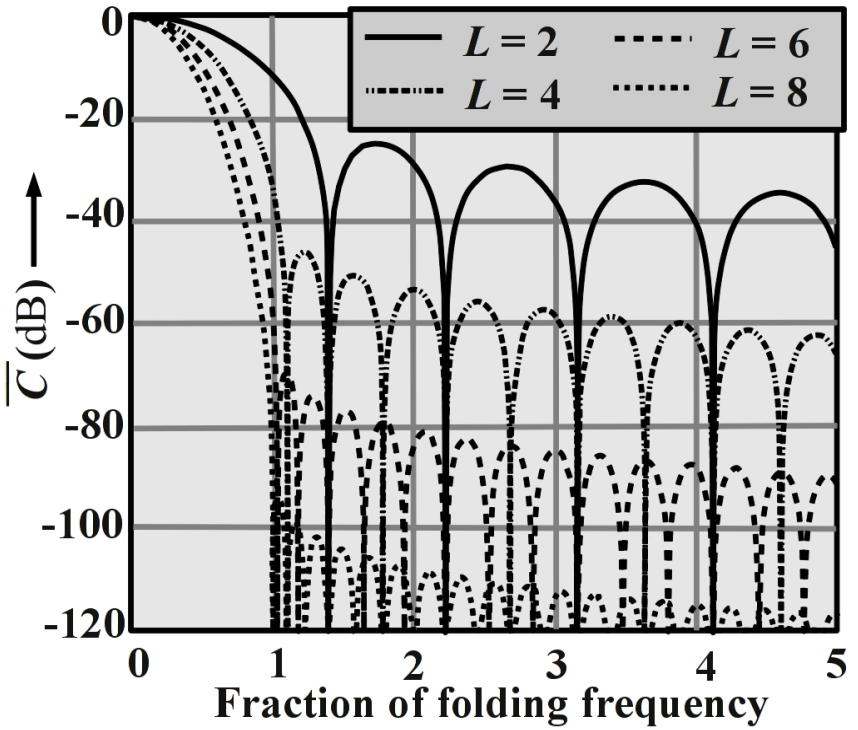

Fourier transform of left figure.

It can be seen that as L increases, the performance of the function as measured by rejection beyond the folding frequency improves.

Dirty Image from Inverse Fourier Trans.-I

We reproduce Eq. (22) which represents the measured-calibrated-weighted visibility as:

$$\mathcal{V}_{\rm mcw}(u,v) = \mathcal{V}(u,v)\, W(u,v)\, w(u,v) \quad \text{... (22)}$$

We also know that weighting functions are used to obtain (*i*) uniform effective area density as well as (*ii*) tapering. We now denote them separately as $w_{\rm den}$ and $w_{\rm tap}$ respectively for density and tapering. By substituting them in above we get:

$$\left.\begin{aligned} \mathcal{V}_{\rm mcw}(u_i,v_i) &= \mathcal{V}_{\rm mc}(u_i.v_i)\,[w_{\rm den}(u,v)\, w_{\rm tap}(u,v)] \\ &= [\mathcal{V}(u_i,v_i)\, W(u,v)]\,[w_{\rm den}(u,v)\, w_{\rm tap}(u,v)] \end{aligned}\right\} \quad \text{... (63)}$$

The data contain measured-calibrated visibilities only at fixed locations (u_i,v_i), where i = 1,2,3...$N_{\rm vis}$ and $N_{\rm vis}$ represents number of data pairs. After gridding (after convolving with $C(u,v)$ and sampling with comb $(\Delta u,\Delta v)$) and applying weights (density weighting and tapering), the measured calibrated weighted gridded visibility $\mathcal{V}_{\rm mcwg}(u,v)$ can be mathematically shown as:

$$\mathcal{V}_{\rm mcwg}(\Delta u,\Delta v) = [C(u,v) * \{\mathcal{V}(u_i,v_i)\, W(u,v)\, w_{\rm den}\, w_{\rm tap}\}]\, {\rm comb}\,(\Delta u,\Delta v) \quad \text{... (64)}$$

Dirty Image from Inverse Fourier Trans.-II

We know that visibilities appear in complex conjugate pairs symmetric around the origin of the u,v axes. The actual number of visibilities obtained from the telescope is $N_{\rm vis}$. Equal number of complex conjugate data points are generated from this which lie exactly on the opposite side on the u-v plane. For imaging, entire data (measured + generated) are used. Thus, Eq. (64) is re-written as:

$$\left.\begin{array}{c} \mathcal{V}_{\rm mcwg}(\Delta u, \Delta v) = {\rm comb}\,(\Delta u, \Delta v)\, C(u,v) * [\{\mathcal{V}(u_i, v_i) + \mathcal{V}(-u_i, -v_i)\} \\ \{W(u,v)\, w_{\rm den}(u,v)\, w_{\rm tap}(u,v)\}] \end{array}\right\} \quad \ldots (65)$$

The dirty image $I_{\rm D}(l,m)$ is the inverse FFT of above, which after re-organization can be expressed as:

$$\left.\begin{array}{l} I_{\rm D}(\Delta l, \Delta m) = \left[\frac{{\rm comb}(\Delta l, \Delta m)}{\Delta u\, \Delta v}\right] * \left[I(l,m)\, \{\overline{C}(l,m) * \overline{W}(l,m) * \overline{w}_{\rm den} * \overline{w}_{\rm tap}\}\right] \\ \qquad\qquad = \left[\frac{{\rm comb}(\Delta l, \Delta m)}{\Delta u\, \Delta v}\right] * \left[I(l,m)\, P_{\rm syn}(l,m)\right] \end{array}\right\} \ldots (66)$$

Here, $I(l,m)$ represents the actual intensity distribution of the sky. Its relationship with the true visibility $\mathcal{V}(u,v)$ is given as:

$$I(l,m) = \sum_{i=1}^{N_{vis}} \left[\mathcal{V}(u_i, v_i)\, e^{j2\pi(lu_i + mv_i)} + \mathcal{V}(-u_i, -v_i)\, e^{-j2\pi(lu_i + mv_i)}\right] \quad \ldots (67)$$

Dirty Image from Inverse Fourier Trans.-III

The synthesized dirty beam $P_{\rm syn}$ is given as:

$$\left.\begin{array}{c} P_{\rm syn}(l,m) = \overline{C}(l,m) * \overline{W}(l,m) * \overline{w}_{\rm den}(l,m) * \overline{w}_{\rm tap}(l,m) \\ = \int_{-\infty}^{\infty}\int_{-\infty}^{\infty} C(u,v)\, W(u,v)\, w_{\rm den}(u,v)\, w_{\rm tap}(u,v)\, e^{j2\pi(lu+mv)}\, dl\, dm \end{array}\right\} \quad \ldots (68)$$

Note that, $P_{\rm syn}(l,m)$ has been expressed as the Fourier transformation of the product of (*i*) convolution function $C(u,v) = C_1(u)C_2(v)$, (*ii*) spatial sensitivity function $W(u,v)$, and (*iii*) density and tapering weights ($w_{\rm den}$ and $w_{\rm tap}$).

Let us look at Eq. (65) once more...

$$\left.\begin{array}{c} \mathcal{V}_{\rm mcwg}(\Delta u, \Delta v) = {\rm comb}\,(\Delta u, \Delta v)\, C(u,v) * [\{\mathcal{V}(u_i,v_i) + \mathcal{V}(-u_i,-v_i)\} \\ \{W(u,v)\, w_{\rm den}(u,v)\, w_{\rm tap}(u,v)\}] \end{array}\right\} \quad \ldots (65)$$

We define $\mathcal{V}_{\rm grd}(u,v)$ as the convolved sampled gridded true visibility on a uniform grid having a hole size $\Delta u \times \Delta v$ as expressed below:

$$\mathcal{V}_{\rm grd}(\Delta u, \Delta v) = {\rm comb}\,(\Delta u, \Delta v)\, [C(u,v) * \{\mathcal{V}(u_i,v_i) + \mathcal{V}(-u_i,-v_i)\}] \quad \ldots (69)$$

Substituting above in Eq. (65) we obtain:

$$\mathcal{V}_{\rm mcwg}(\Delta u, \Delta v) = \mathcal{V}_{\rm grd}(\Delta u, \Delta v) W(u,v)\, w_{\rm den}(u,v)\, w_{\rm tap}(u,v) \quad \ldots (70)$$

Dirty Image from Inverse Fourier Trans.-IV

From previous slide we have ...

$$\mathcal{V}_{\rm mcwg}(\Delta u, \Delta v) = \mathcal{V}_{\rm grd}(\Delta u, \Delta v) W(u,v)\, w_{\rm den}(u,v)\, w_{\rm tap}(u,v) \quad \text{... (70)}$$

By performing an inverse FFT operation on above equation, the discrete image $I_{\rm D}(l_i,m_i)$ is obtained as:

$$\left.\begin{aligned} I_{\rm D}(l_i, m_i) &= I_{\rm grd}(l_i, m_i) * P_{\rm syn}(l_i, m_i),\ \ l_i, m_i = 0, \pm 1, \pm 2 \ldots \\ &= \sum_{l_i'=-\infty}^{\infty} \sum_{m_i'=-\infty}^{\infty} [I_{\rm grd}(l_i, m_i)\ P_{\rm syn}(l_i - l_i', m_i - m_i')] \end{aligned}\right\} \quad \text{... (71)}$$

Here $P_{\rm syn}(l_i,m_i)$ represents an equally spaced (gridded) weighted discritized synthesized dirty beam.

Image Improvement by Deconvolution-I

However best be the applied tapers and weights, side-lobes always exist in the synthesized beam resulting in artifacts on the dirty image. Hence, they must be removed by additional processes. They involve several deconvolution and convolution operations on the dirty image I_D. In its most simplified form shown below, I_D is a convolution between the true image I and the dirty beam P_D.

$$I_D = P_D * I \qquad \ldots (72)$$

To recover the true image I, a deconvolution process of the form shown below may be used, where the operators $\mathcal{F}$ and $\mathcal{F}^{-1}$ respectively represent Fourier and inverse Fourier transforms.

$$I = \mathcal{F}^{-1}\left[\frac{\mathcal{F}[I_D]}{\mathcal{F}[P_D]}\right] \qquad \ldots (73)$$

This process is known as ***linear deconvolution***. This method gives a good understanding of the noise properties and it is computationally cheaper. However it is not suitable for radio interferometry since the *u-v* plane has a high population of zeros due to limited baselines. The next alternative is to use ***non-linear deconvolution*** algorithms.

Image Improvement by Deconvolution-II

In a non-linear deconvolution, the unmeasured parts of the Fourier plane are filled with a plausible distribution based on the properties of the real sky. The logic comes form the appearance of the sky, which does not show any features of the dirty beam like rings, spokes, negative regions and a finite sky extents. Two popularly used algorithms known today are:

(*i*) CLEAN.
(*ii*) MEM

The above are described next.

Image Improvement: CLEAN Algo-I

The response of a telescope when focussed to a point source is known as ***point spread function*** (PSF) which is our synthesized beam.

The image can be thought to composed of several point sources. Each of these sources can be constructed with individual PSF. The iterations involve locating their positions, finding their strengths and attenuating them as illustrated. These steps are summarized in next slide...

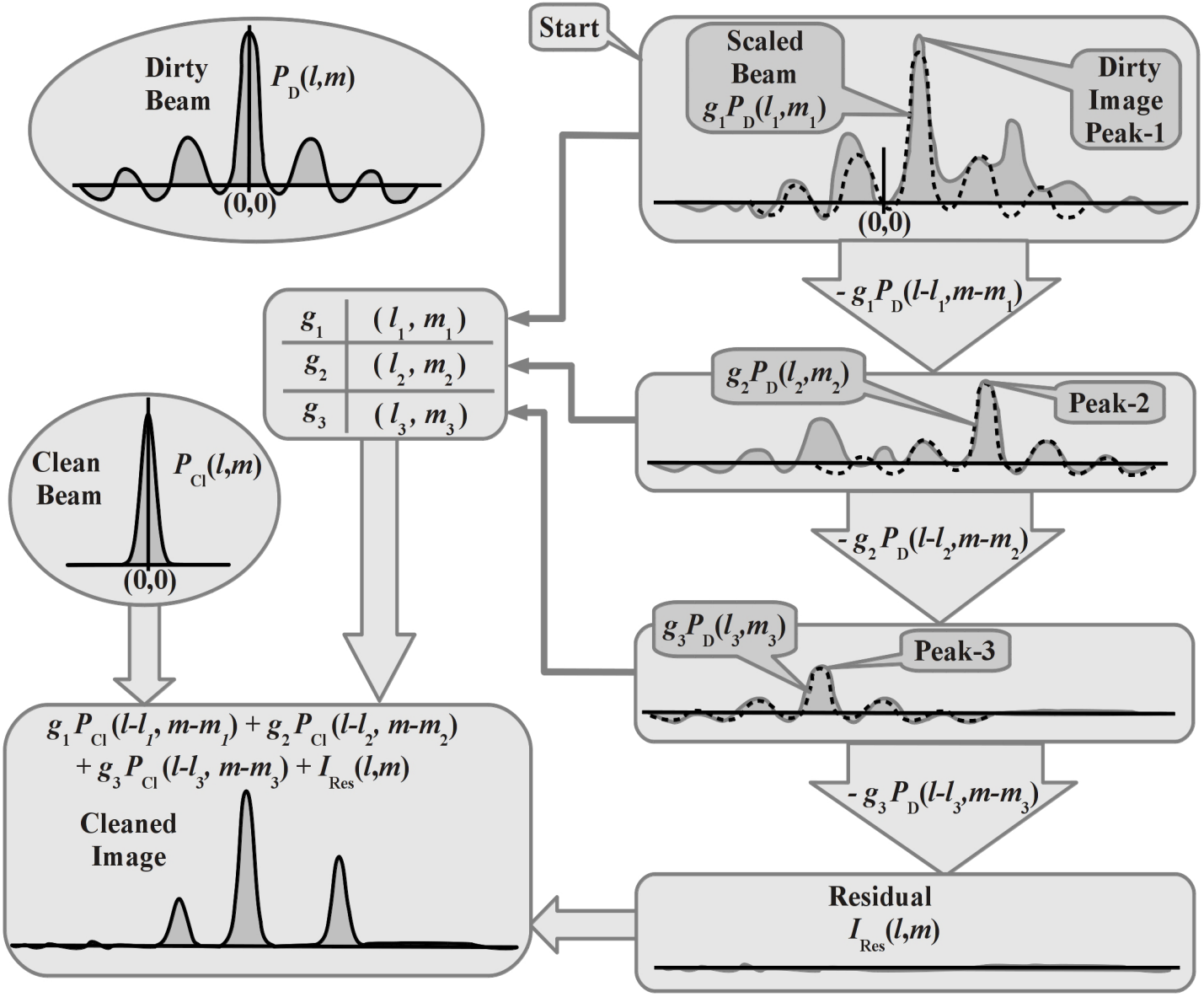

Image Improvement: CLEAN Algo-II

(*i*) In every iteration, the absolute strength and position (l_0,m_0) of the most brilliant peak in the dirty image $I_D(l,m)$ are determined.

(*ii*) The dirty beam $P_{syn}(l,m)$ is multiplied by a gain factor g usually having a value lying between 0.1 and 0.25 resulting in a weighted dirty beam $g\times P_{syn}(l,m)$.

(*iii*) The weighted dirty beam $g\times P_{syn}(l,m)$ is shifted to (l_0,m_0) for alignment with the peak of the dirty map, and then subtracted from it. In the process, the side-lobes are also subtracted.

(*iv*) Amplitude and position of the removed component are recorded separately in the CLEAN model. This is done by introducing a delta function (having same gain) at that location.

(*v*) Iteration steps (*ii*), (*iii*) and (*iv*) are repeated again and again until the remaining peak goes below a specified value.

(*vi*) The CLEAN model obtained from the accumulation of point sources by the iterations is convolved with an ideal beam having no side-lobes (usually a Gaussian beam) which produces the CLEAN image.

(*vii*) Residuals from subtractions in the dirty image are next added to the CLEAN image.

Image Improvement: CLEAN Algo-III

Effectively, CLEAN removes the image contents produced by the side-lobes. The quality of a CLEAN image depends on the user. Details of a radio image with CLEAN applied is shown below.

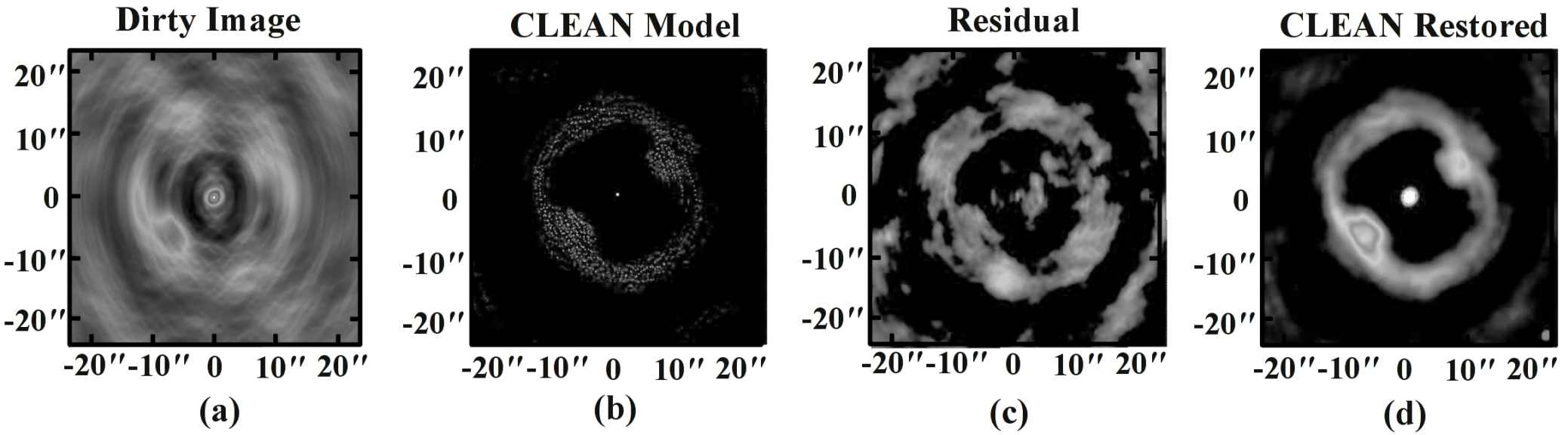

Figure: Application results of CLEAN algorithm.

(a) Original dirty image.
(b) Model of point sources chosen for applying CLEAN.
(c) Residuals from the image after applying CLEAN.
(d) Restored CLEAN image.

MEM (Maximum Entropy Method) Algo-I

Unlike the entropy described by information theory which is a measure of the uncertainty associated with a random variable, the entropy described for use in imaging is different. Let $I_{\mathrm{M}}(l,m)$ represent a sky intensity distribution obtained using MEM and let $F(I_{\mathrm{M}})$ be its entropy as expressed below.

$$F(I_{\mathrm{M}}) = -\int I_{\mathrm{M}}(l,m)\,\log\left(I_{\mathrm{M}}(l,m)\right)\,dl\,dm \qquad \ldots (74)$$

Note that $F(I_{\mathrm{M}})$ has also been defined in slightly different ways by the users.

The basic idea is to maximize $F(I_{\mathrm{M}})$ of the optimized image. An initial model of the source is chosen with assumption that the sky is uniform and positive. The process starts with this model. Let k represent all the discrete visibility points in the data. Let the measured visibilities be represented as $\mathcal{V}_k^{\mathrm{meas}}(u_k,v_k)$ and let $\mathcal{V}_k^{\mathrm{model}}(u_k,v_k)$ represent those of from the model. Let ξ^2 be a measure of their mean square differences as expressed below, where σ_k^2 represents the noise variance.

$$\xi^2 = \sum_k \frac{\left|\mathcal{V}_k^{\mathrm{meas}} - \mathcal{V}_k^{\mathrm{model}}\right|^2}{\sigma_k^2} \qquad \ldots (75)$$

MEM (Maximum Entropy Method) Algo-II

Many optimization algorithms have been used. One such is expressed below, where α and β are Lagrange multipliers and S_{model} represents the model's total flux-density. To get an optimized solution, the quantity J should be maximized.

$$J = F(I_M) - \alpha\xi^2 - \beta S_{\text{model}} \quad \ldots (76)$$

The values of α and β are adjusted during the iteration so that ξ^2 and S_{model} are same as their expected values. Details of a radio image with MEM applied is shown below.

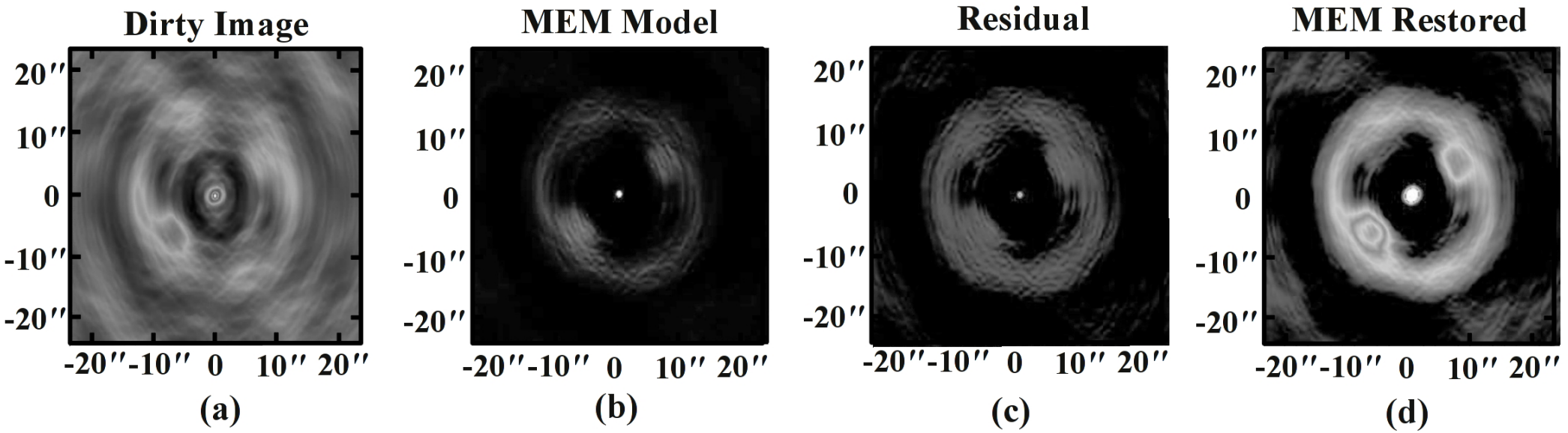

Above: (a) The original dirty image. (b) Model point sources chosen for applying MEM. (c) Residual of the image after applying MEM. (d) The MEM restored image.

CLEAN vs. MEM

The CLEAN works well on compact sources while the MEM is more useful for extended sources. Unlike MEM, CLEAN is easy to understand and robust. However, when applied on extended sources, it introduces corrugations in the deconvolved image provided there are strong side-lobes in the dirty beam. The short baselines gives more information about the source intensity if it is large or extended. Absence of short baselines can create a negative bowl (explained later) since the zero level in the image varies with position. This makes CLEAN unsuitable for large structures. MEM handles these very well.

Some of these problems are solved using the Multi-Resolution CLEAN (MRC) technique where the image is smoothened to a lower resolution and a difference is created between the dirty image and smoothened image. These are separately deconvolved using the smoothed and difference beams and results are related so that the fine-scale structures are retained.

Other Methods

In another approach dirty images of different resolution are made using wavelet transforms. These are then separately deconvolved and restored like MRC. However, this has a relatively rigorous framework than MRC.

In another approach for deconvolution, a linear system of equations **AX** = **B** can be formed, where **A** represents the samples of the dirty beam, and **B** represents the samples of the dirty image, while **X** represents the components of reconstructed image. Solution methods from linear algebra can be adopted for finding **X**. However, since **A** is singular, additional information are required for a solution. Methods like the Non-Negative Least Squares (NNLS) may be for a solution. Unlike the iteration type of decovolutions, this approach gives a direct solution.

Imaging using Wide Frequency Bands-I

In order to use wide band-widths in imaging, we have to understand its functionality. We first try to understand the effects of wide band-widths.

Let a source at CNP be observed at two wavelengths λ_1 and λ_2 having a common baseline distance d. The data appear as circles on the u-v plane having radii r_1 and r_2 given as:

$$r_1 = d/\lambda_1 \qquad r_2 = d/\lambda_2$$

$$r = \frac{length}{\lambda}$$

$$\lambda_1 > \lambda > \lambda_2$$

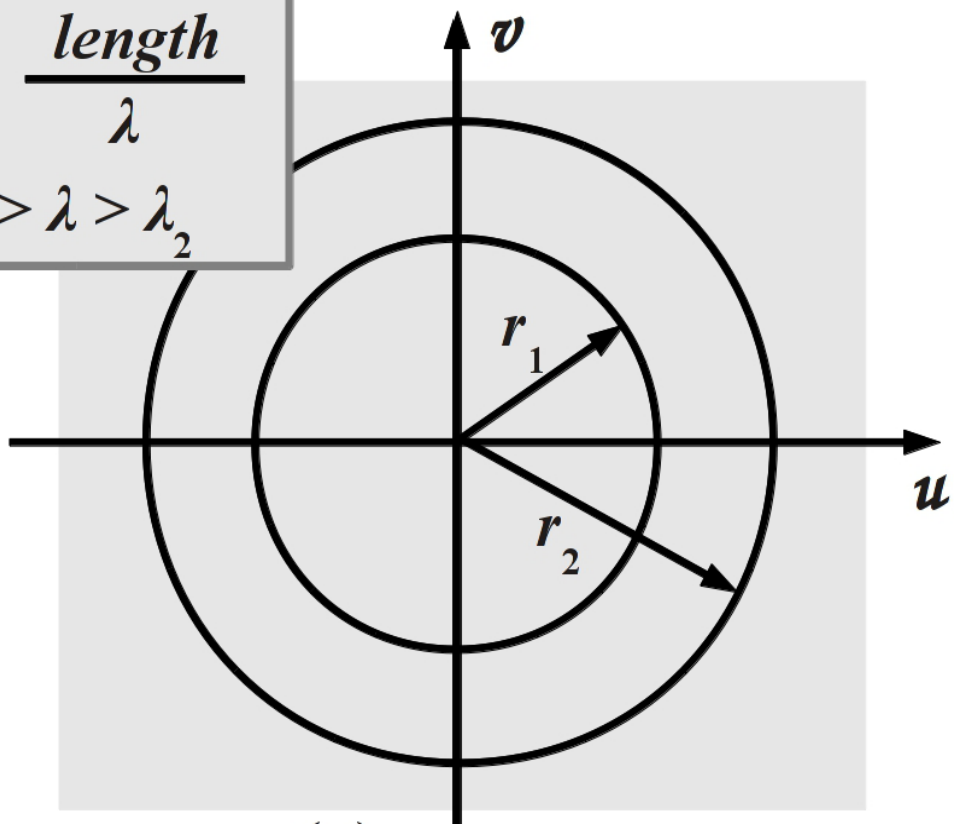

For the two frequencies, the baselines are different. If system's cut-off frequencies are c/λ_1 and c/λ_2, where c is the speed of light, the visibility will contain all information between these frequencies.

Imaging using Wide Frequency Bands-II

$$r_1 = d/\lambda_1 \qquad r_2 = d/\lambda_2$$

However, the correlator may produce a single integrated output corresponding to the whole band. Effectively, the correlator's integrator will merge the data and place it on the average baseline given as $(r_1 + r_2)/2$. In other words, the visibility function is smeared. This effect also known as ***band-width smearing***, and can severely affect the image especially for large system band-widths.

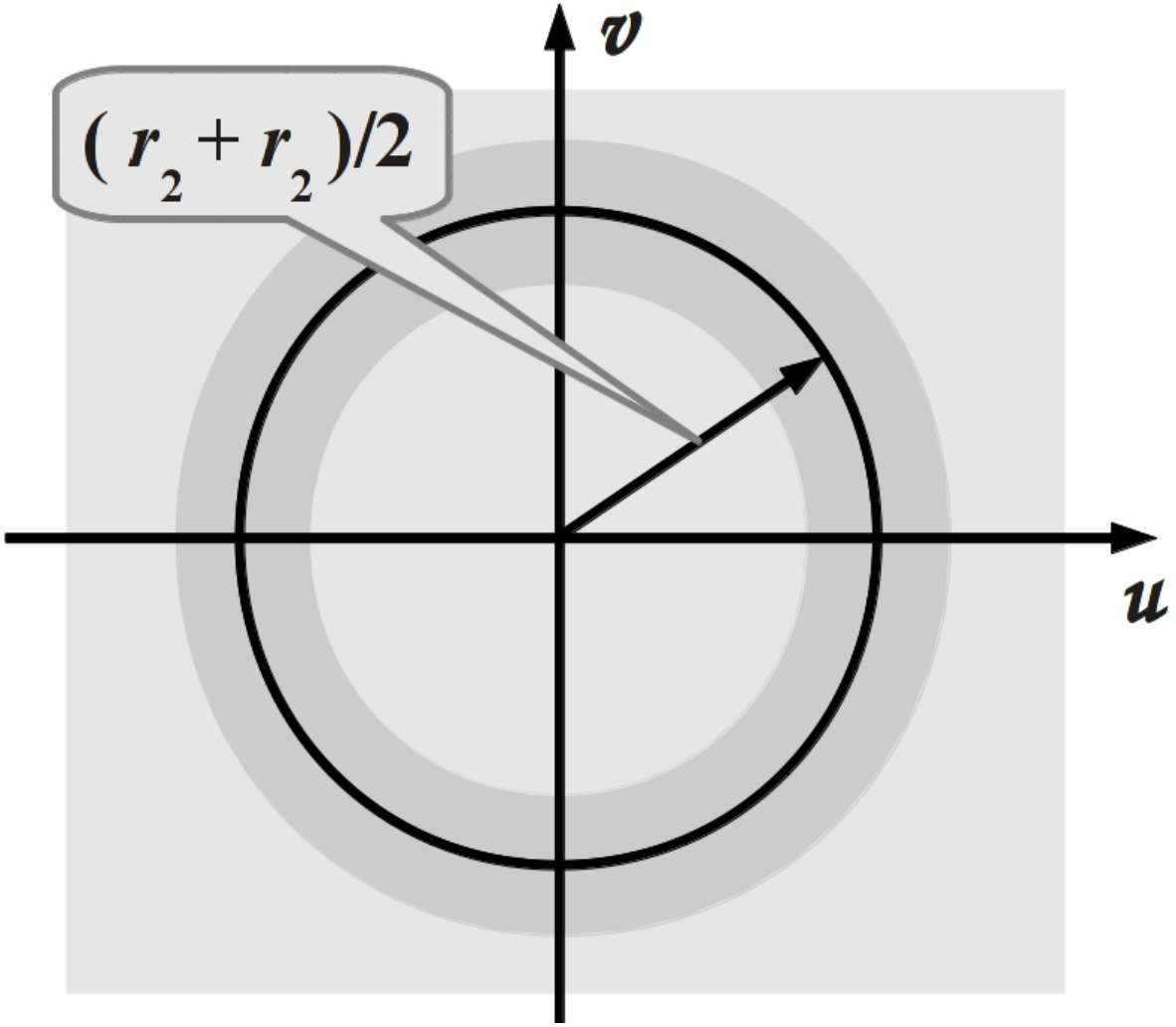

Conclusion: It is possible to densely populate the *u*-*v* plane more densely with the same instrument if its frequency resolution is improved.

Wide-Field Imaging

The field of view of the primary beam of a dish antenna is determined by its physical aperture area or diameter. Similar is the case of a synthesized aperture using visibilities obtained from an interferometer array where the main beam is determined from the *u-v* coverage. Whereas, for an interferometer, the angular resolution depends on the projected distance of separation between the two antennas. The sensitivity in all the three cases decreases with increase in angular distance from the center of the field of view. The figure shows this for an interferometer and a single dish.

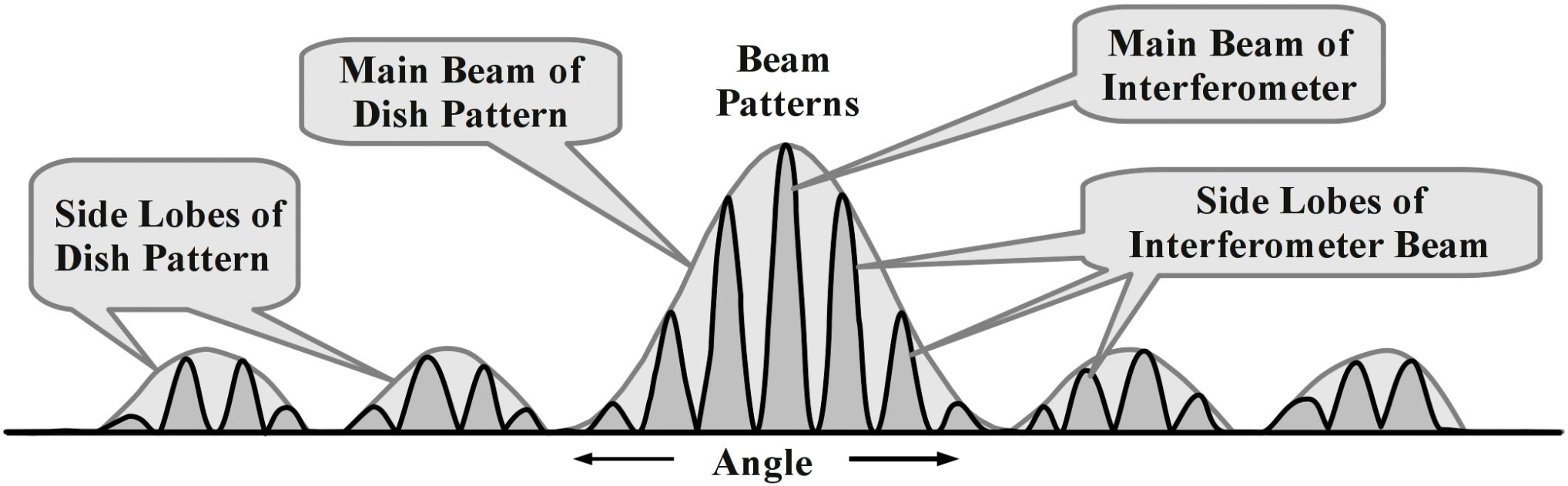

Wide-Field Img.: Short Baselines Absent-I

The possible minimum distance d between two antennas of an interferometer is equal to the diameter D of a single dish (assuming both the dishes have same diameter). Hence the smallest baseline possible in any interferometer array is D. The observer expects a u-v plane coverage from an interferometer array for full observation time to look like a wide pulse in one dimension as shown below, where the width of the pulse is equal to the largest baseline in the array. The synthesized beam from this data would be a narrow sinc function.

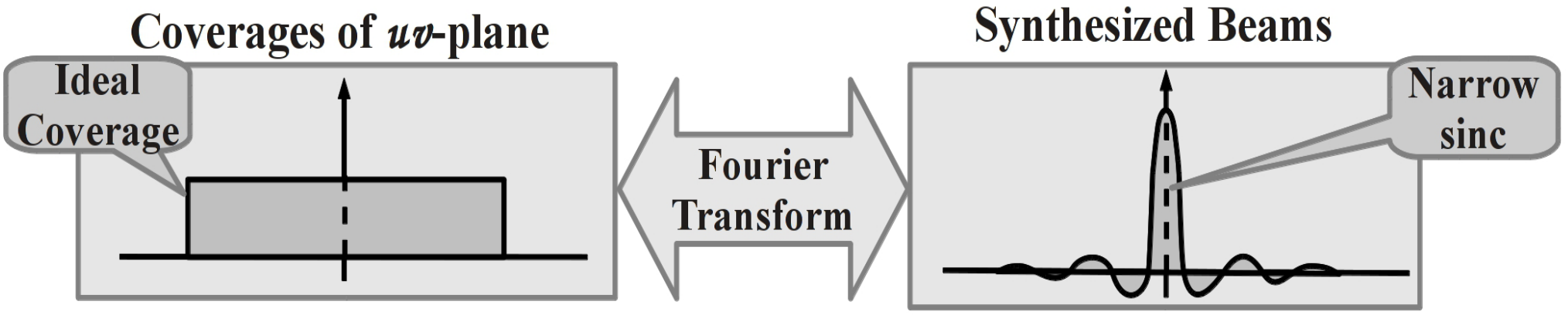

Wide-Field Img.: Short Baselines Absent-II

The spatial frequency components produced from a single dish is from 0 to D/λ. However, they are not separable and appear as a single value. If the dish is treated as composed of several interferometers, such that it produces spatial frequencies ranging from 0 to D/λ, which when plotted should look like a narrow pulse as shown below. For an interferometer array, this pulse is is missing since the minimum possible projected baseline is D/λ. Hence the broad sinc component produced by this in the synthesized beam is also missing.

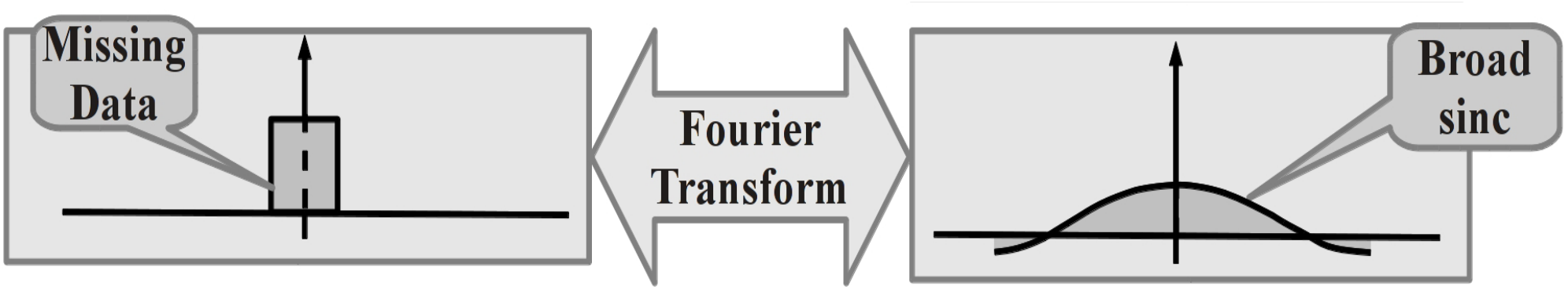

Wide-Field Img.: Short Baselines Absent-III

The actual interferometer *u-v* coverage looks like as shown. Note that the central part (short spacing) data is missing. The effects are undesirable as the synthesized beam contains a modulated sinc function. The narrow sinc function is modulated by the wide sinc function. Observe that in the central region, the beam has been pulled in the negative direction. This effect is know as negative bowl. This problem is also known as ***short spacing problem***.

Wide-Field: Soln. to Short Baseline Prob.

The spatial frequency components available from a dish of diameter D is from 0 to D/λ. If in some way we are able to separate these components so that they actually cover the u-v plane with spatial frequencies from 0 to D/λ, we may combine with it the data obtained from an interferometer array. From practical view point, a separate dish having a diameter greater the D is required for reasons described below.

If $d_{\lambda(\min)}$ is the shortest baseline of an interferometer array, then the theoretical minimum diameter of the additional single dish required is $D_{sd} = d_{\lambda(\min)}$. However, we are aware that practical dish illuminations by antenna-feeds are non-uniform and reduce at the edges of the dishes as shown. This results in attenuation of the higher spatial frequency components (towards the edges of the dishes). Hence for all practical purposes, a larger diameter dish is chosen, usually with a diameter $D_{sd} = 2\ d_{\lambda(\min)}$. This gives an overlap region between single dish data and interferometer data which is useful for cross-calibrations between the two.

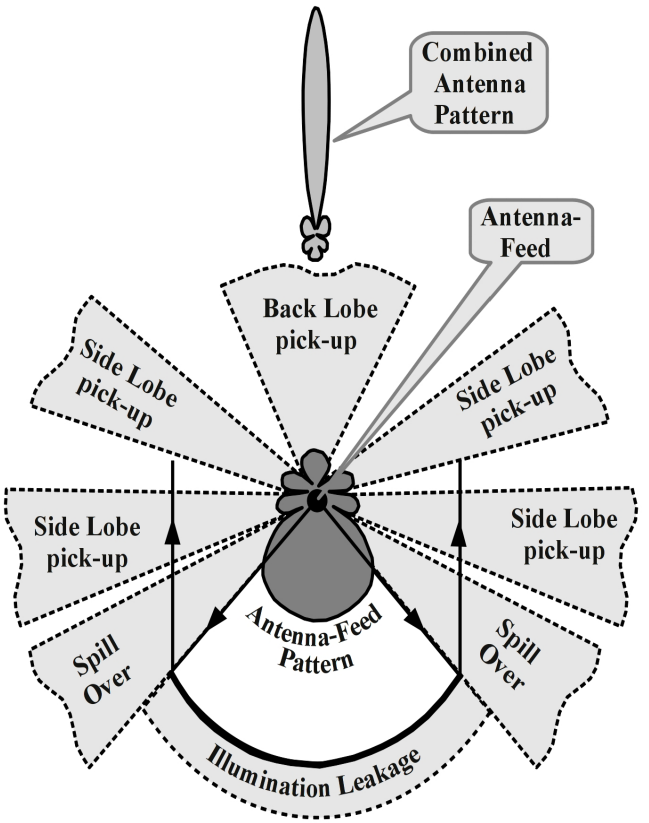

Single Dish as Multiplicative Interferometer

A single dish data may be visualized as a auto-correlation component while combining with any interferometer data.

An interferometer's output is $G^2 < v_1 v_2 >$, where G is the gain of each amplifier, and v_1 and v_2 are the antenna signal voltages. The symbol <> represents averaged over time. The instrumental time delay for phase adjustment is represented by τ_i.

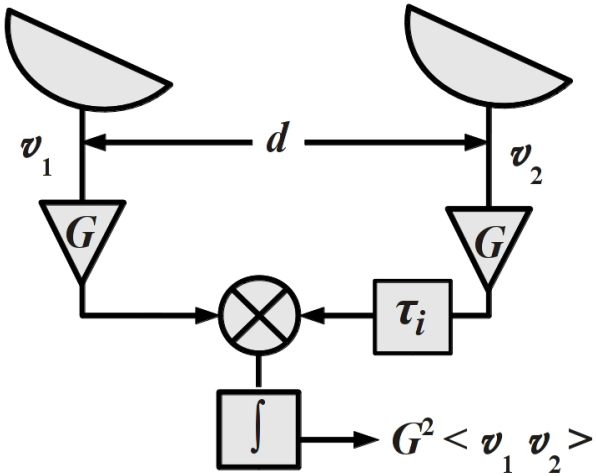

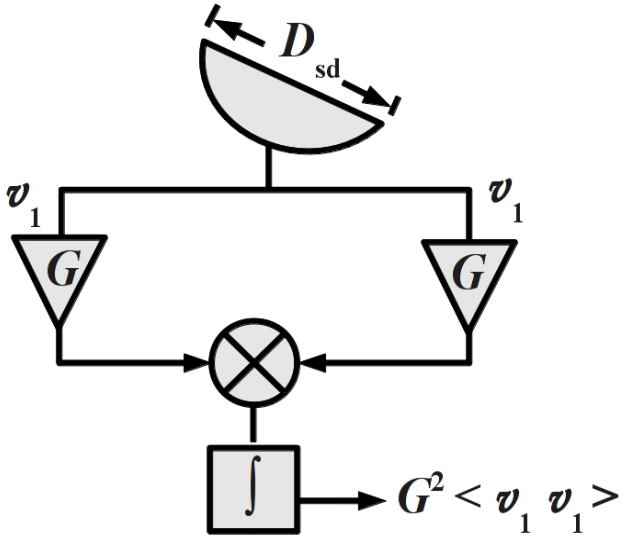

As a special case, when where $v_1 = v_2$, the same configuration takes the form shown on left. This may further be simplified to as shown on right.

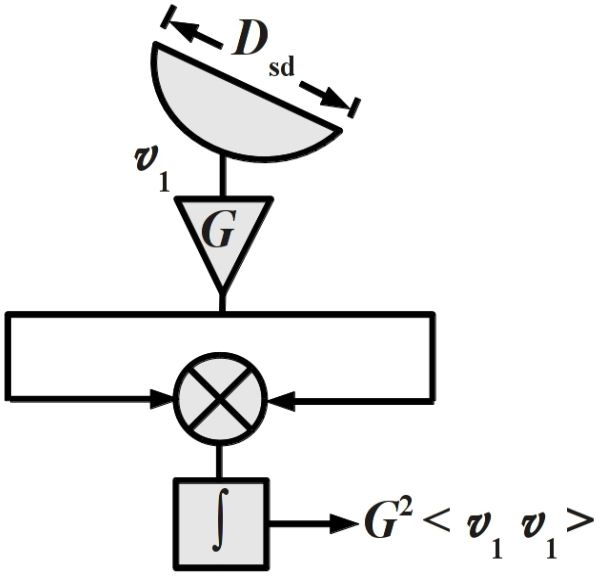

Recall Sampling Theorem of Observing Angle

One dimensional Sampling Theorem

An observed distribution is completely determined by measurements spaced at equal discrete intervals which are at least as narrow as $1/2s_c$, where s_c is the *cut-off spatial frequency* of the antenna aperture.

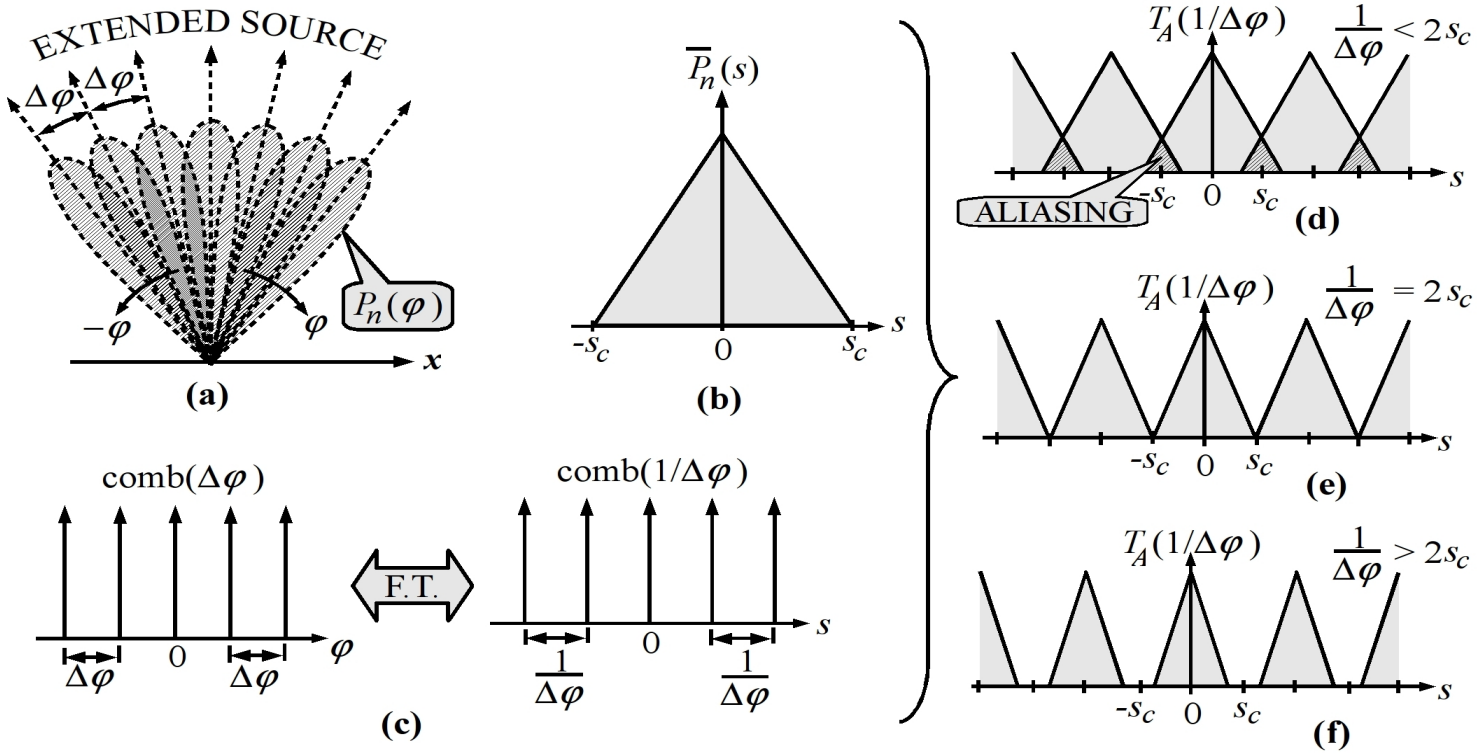

(a) Scanning extended source at angular intervals $\Delta\varphi$. (b) Spatial antenna spectrum. (c) Discrete angular observation points and spatial Fourier transform. (d) Large angular scanning interval (aliasing). (*e*) Optimum scanning interval (true spectrum). (f) Small scanning interval (over sampling).

Generating *u*,*v* data from Single Dish-I

Single dishes can be used to observe extended objects whose angular size is greater than $1.22\lambda/D_{sd}$, where D_{sd} is the diameter of the dish.

Let a square region of the sky contain an extended source. Divide this region by the beam-width of the single dish so that a equallyspaced squares are created. The center of each of squares are marked with '+' sign. The dish is now pointed at each of these locations and data is taken. Hence we have scanned the extended object at angular intervals of the beam-width of the single dish based on the sampling theorem of observing angle.

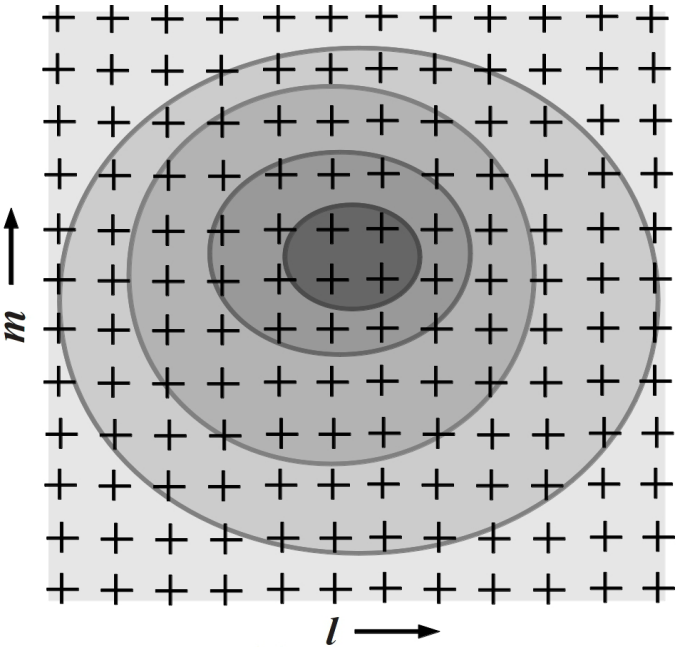

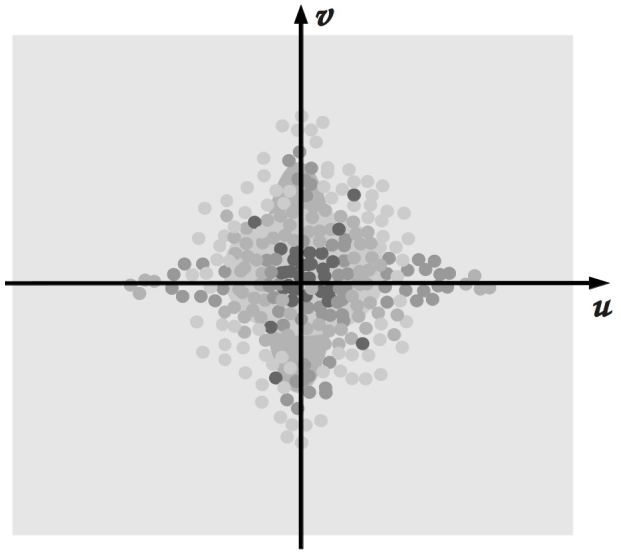

The Fourier transform of this data generates the visibility components on the *u*-*v* plane. Note that the data resides in the mid section of the *u*-*v* plane which means they are the lower spatial frequency components.

Generating *u,v* data from Single Dish-II

Let us divide the aperture area of a single dish into a finite number of small areas. Each of these may be treated as apertures of small independent antennas. Assume an interferometer-like baseline between any two such elements (shown with double headed arrow). The maximum possible size of this baseline is the diameter D_{sd} of the dish. The number distribution of these baselines is shown below:

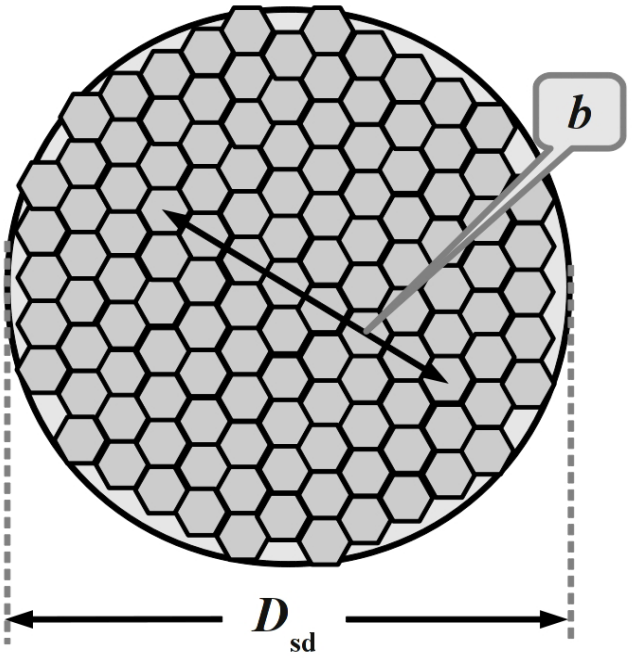

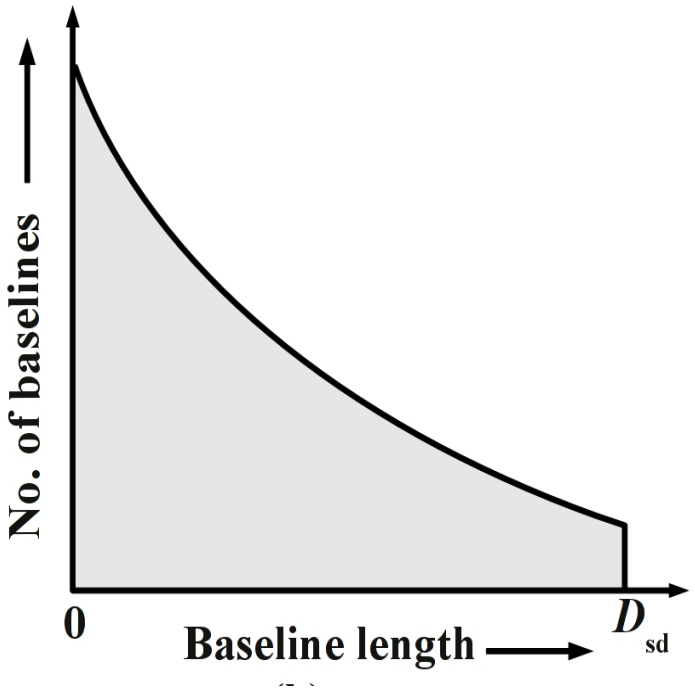

If $P_{sd}(l',m')$ represents the beam pattern of the single dish, then the observed sky brightness $I_{sd}(l,m)$ using the dish can be shown as:

$$I_{sd}(l,m) = I(l,m) * P_{sd}(l',m') \quad \ldots (77)$$

Here $I(l,m)$ is the true intensity distribution on the sky. The dummy coordinates l',m' are used to denote the movement of the antenna while scanning the sky at discrete angular intervals.

Generating *u,v* data from Single Dish-III

From last slide we have ...

$$I_{\rm sd}(l,m) = I(l,m) * P_{\rm sd}(l',m') \quad \ldots (77)$$

Applying a Fourier transformation to above equation we obtain the observed single dish visibilities $\mathcal{V}_{\rm osd}(u,v)$ as shown below, where $\mathcal{V}_{\rm sd}(u,v)$ are the true visibilities and $W_{\rm sd}(u,v)$ is the spatial sensitivity function of the single dish.

$$\mathcal{V}_{\rm osd}(u,v) = \mathcal{V}_{\rm sd}(u,v)\, W_{\rm sd}(u,v) \quad \ldots (78)$$

Note that determination of $I(l,m)$ from $I_{\rm sd}(l,m)$ has to be done by deconvolution. However, no interpolations are required on $\mathcal{V}_{\rm osd}(u,v)$ since it is continuous across the *u-v* plane.

Adding Single Dish with Interferometer-I

We know that *u-v* data obtained from an interferometer always contain as hole in the center as shown on right. The *u,v* data obtained using a single dish covers the central region of the *u-v* plane as shown below.

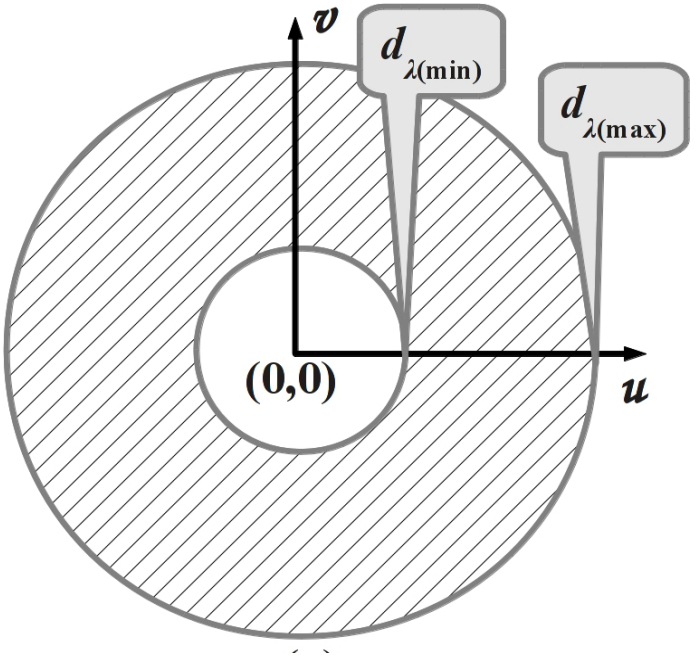

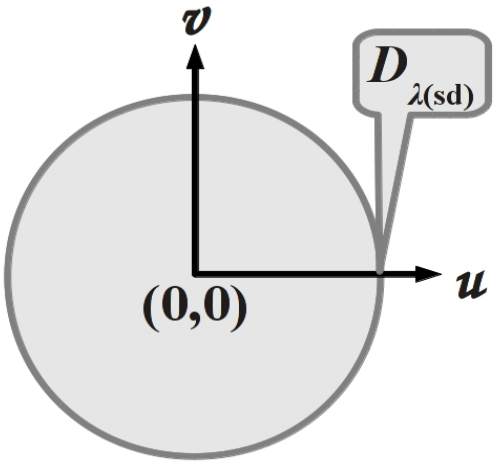

$$D_{\lambda(sd)} = D_{sd}/\lambda$$

The size of the single dish is chosen such that there is an overlapping region between the two data sets as shown on the right. Relative calibrations between the two is made in this region.

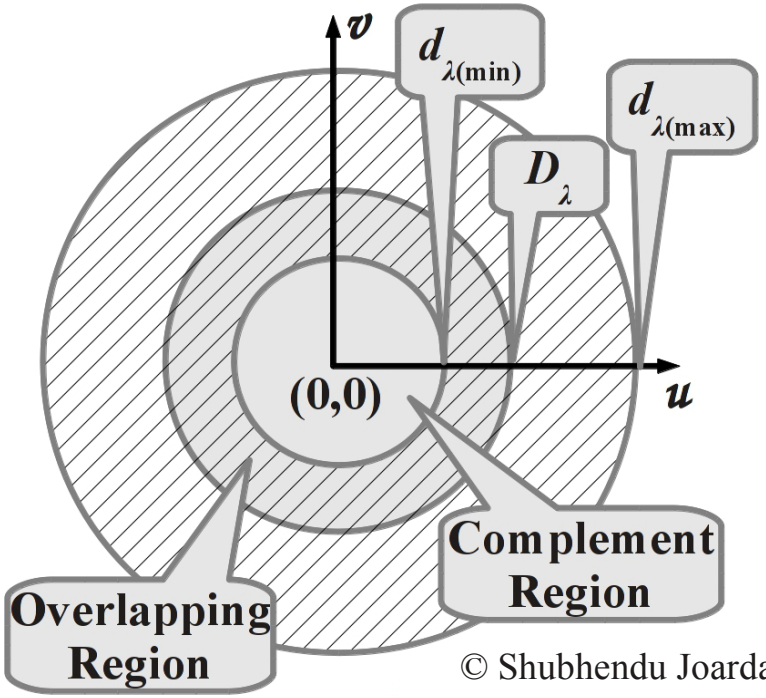

Adding Single Dish with Interferometer-II

Let K_{cal} be the calibration ratio of flux densities of an unresolved source in the maps obtained by an interferometer and a single dish as expressed below, where S_{int} and S_{sd} respectively represent the flux densities obtained from interferometer and single dish.

$$K_{cal} = \frac{S_{int}}{S_{sd}} \quad \ldots (79)$$

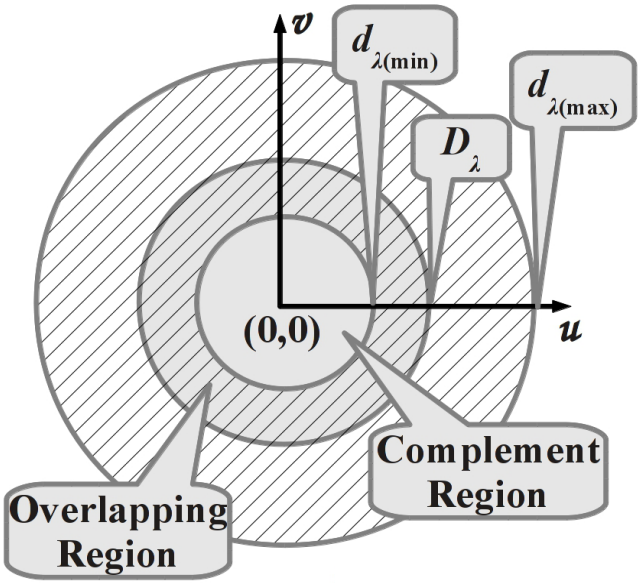

For a source having a brightness I, intensities measured by both the single dish (I_{sd}) and interferometer (I_{int}) should measure same within this region. The calibration ratio K_{cal} is now given as:

$$K_{cal} = \frac{I_{int}}{I_{sd}} \quad \ldots (80)$$

The beam-widths of an interferometer (Ω_{int}) and a single dish (Ω_{sd}) are not same. Hence, for extended sources, the quantities I_{sd} and I_{int} are usually expressed in units of flux-density per beam-width (jansky/beam) instead of flux-density per solid angle (jansky/steradians). The resolution ratio between the two is given as:.

$$\alpha = \frac{\Omega_{int}}{\Omega_{sd}} \quad \ldots (81)$$

Adding Single Dish with Interferometer-III

To find the value of K_{cal} the following steps are performed:

- Using α scale the single dish data and eliminate the difference in brightness due to different beam-widths.
- Apply Fourier transformations to both images (from single dish and interferometer). Be careful about edge effects. Reduced them by applying a smooth tapering of the image intensities towards the edges.
- Obtain the true visibilities $\mathcal{V}_{sd}$ by deconvolving the single dish data (divide the observed visibilities $\mathcal{V}_{osd}$ with the spatial sensitivity function W_{sd} (Eq. (78))). Since W_{sd} is the Fourier transform of the single dish beam (P_{sd}), a good knowledge about the beam of the single dish is required before performing this step.
- Compare the visibilities in overlapping region in the u-v plane. For a Gaussian tapered dish illumination, for a cut-off level of 0.2, the minimum diameter $D_{sd(min)}$ is expressed below, where d_{min} is the shortest baseline distance in the interferometer data. The SNR of single dish visibilities within the overlapping region should be comparable to those of interferometer, else map quality may degrade. After intercalibrations, the data may be combined.

$$D_{sd(min)} > 1.5\, d_{min} \quad \ldots (82)$$

Mosaicking-I

Mosaicing is a technique by which a portion of sky larger than the primary beam of interferometer array elements can be mapped.

Let a small rectangular portion of sky have a non-uniform temperature distribution. Divide this region by the primary beam-width of the interferometer elements so that equally spaced squares are created whose centers are marked with a '+' sign. The array is pointed to each of these locations and data are collected. The principle is based on the sampling theorem of observing angle.

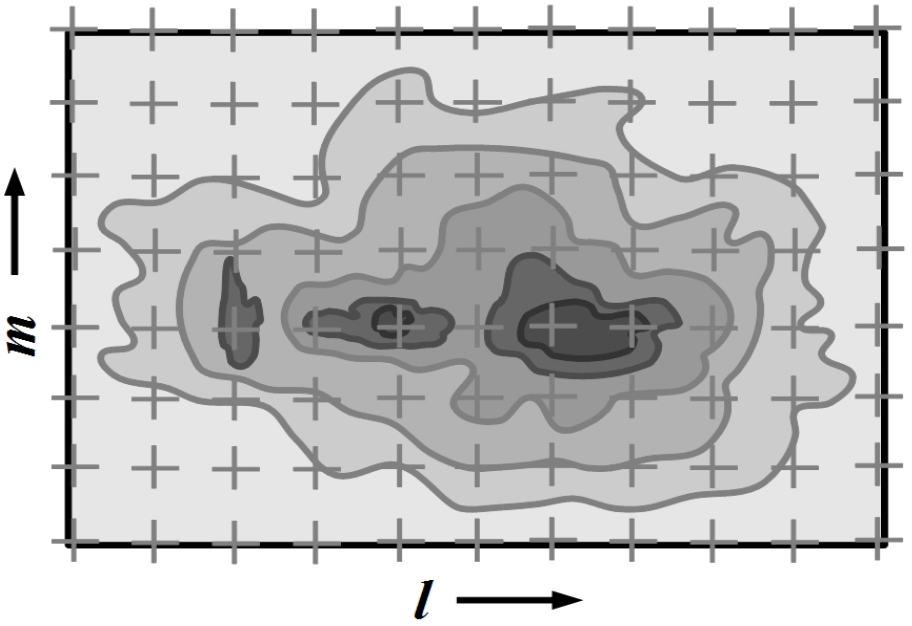

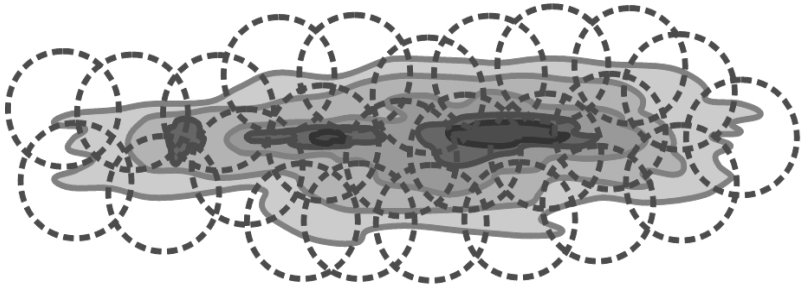

For observing an extended source or arbitrary shape, the scanning can be done as shown on left, where the circles represent the extent of the primary beams.

The entire process of mosaicking can be described in three steps, which are listed in the next slide.

Mosaicking-II

(*i*) Obtain the visibilities for an appropriate series of pointing centers.

(*ii*) Produce a series of maps by independently reducing the data. Each of these maps cover approximately the primary beam solid angle of an antenna element. Non-linear deconvolution algorithms like CLEAN or MEM may be used for removing the effects of side-lobes in the individual Images.

(*iii*) Combine these maps together like mosaics to obtain the complete scanned view.

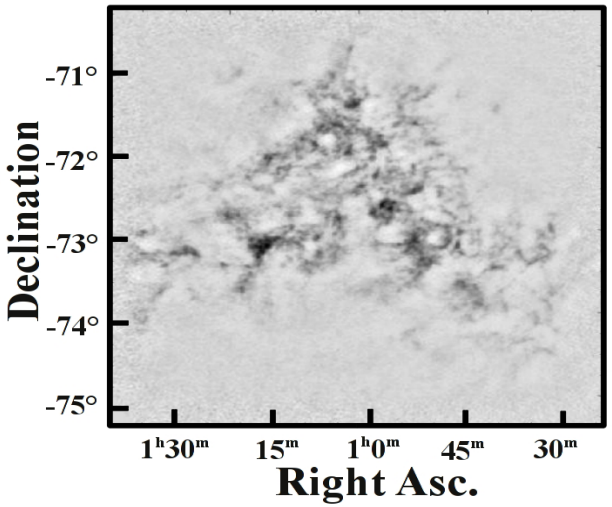

A mosaicked image obtained by using interferometer alone.

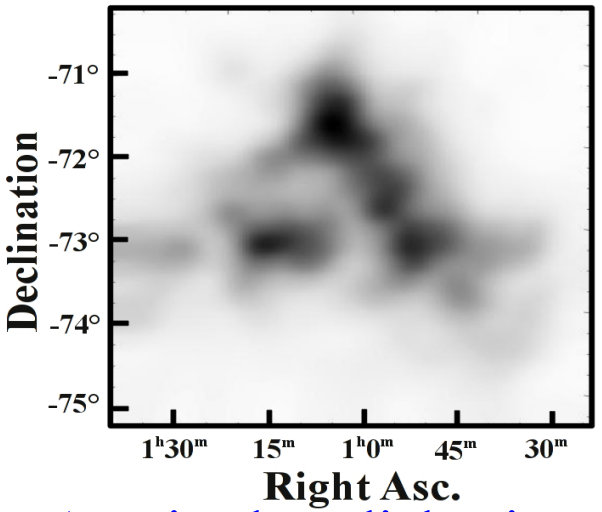

A single dish image. Contains lost information (negative bowl).

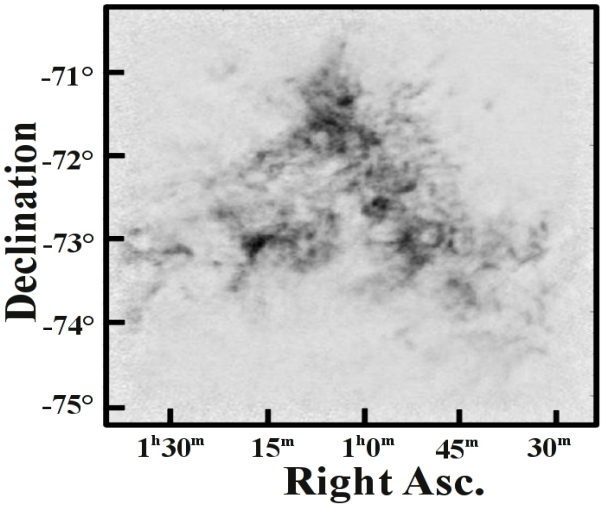

Image from combined data. (Stanimirovic et al, 1999).

Interferometer image has finer details. Single dish image has coarse details. Combined image has full information.

WF Imaging: Non-Coplanar Baselines-I

Mosaicking can cover a large field of sky view. There are also other methods for which, we must understand the concepts of planar and non-planar baselines. We must also understand why conventional imaging method may not be a good choice for wide-field imaging.

Coplanar baselines remain in a fixed plane during the entire observation period. Here we are talking only about baselines and not projected baselines. If the antennas are positioned strictly along the East-West lines, and they are possess identical altitudes, only then we obtain coplanar baselines for entire observation period irrespective of the source position on the sky.

The disadvantages of using East-West baselines is that 2D Fourier mapping becomes difficult if the source is near the celestial equator. Hence, most interferometer arrays are made such that there exists some baseline components along North-South directions. However, this makes the baselines non-coplanar, since they do not remain on a fixed plane as a function of time due to Earth rotation.

WF Imaging: Non-Coplanar Baselines-II

An interferometer is pointed to zenith. Its projected baseline is co-planar to the baseline since both lie on the u-v plane (v-axis is perpendicular to page). The extended source is measured using θ or l. Thus, $l = \sin\theta$ and $n = \cos\theta$. But $w = 0$ since antenna plane coincides with the plane of projected baseline. If visibility phase φ is zero towards the source, we get:

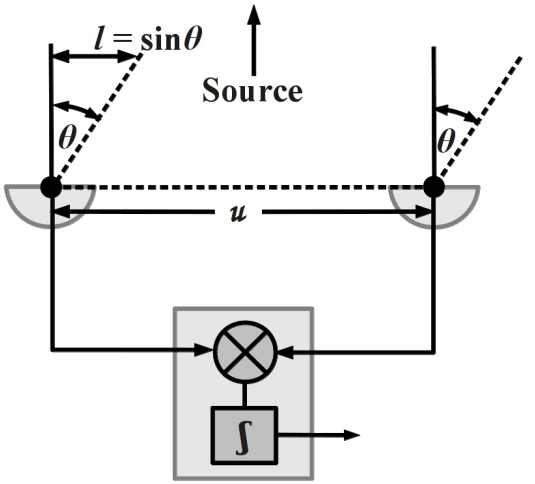

$$\phi = 2\pi ul \quad \text{... (83)}$$

If one antenna is at a higher altitude, the baseline is not on the u-v plane and $w \neq 0$. In this case the phase φ at an angle θ from the zenith is given as:

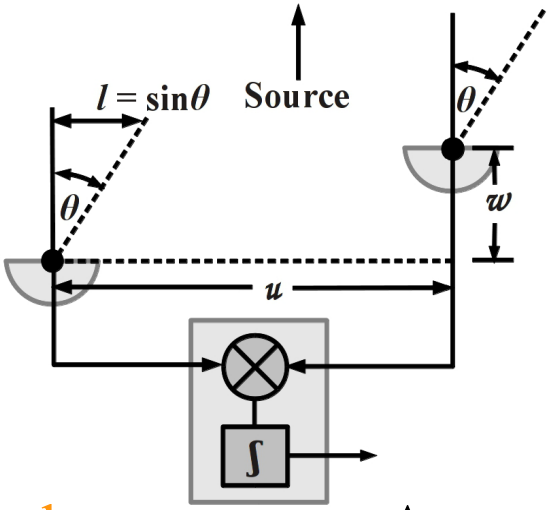

$$\phi = 2\pi\left[ul + w(n-1)\right] \quad \text{... (84)}$$

Note that φ is not same except when $\theta = 0$. The additional component $\Delta\varphi = w(n\text{-}1)$ is dependent both on w and θ. The correct phase of the source extent is given by Eq. (83) which means the we should have baselines co-planar with the u-v plane. This situation seldom occurs since there exists North-South baseline components in most of the radio arrays, and also the antennas may not be at same altitude.

WF Imaging: Non-Coplanar Baselines-III

The approximated van Cittert-Zernike equation does not support wide field imaging. So we reproduce the original equation (Eq. (1)) as shown below:

$$\mathcal{V}(u,v,w) = \int_{-\infty}^{\infty}\int_{-\infty}^{\infty} \frac{P_n(l,m)\, I(l,m)}{n}\, e^{-j2\pi[ul+vm+w(n-1)]} dl\, dm \quad \ldots (85)$$

This general relationship may be seen as some sort of a 3D Fourier like transformation of $\mathcal{V}(u,v,w)$, giving a 3D image volume $F(u,v,w)$ which may be somehow related with the intensity $I(l,m)$. It is given below:

$$\left.\begin{array}{c} F(u,v,w) = \iiint \mathcal{V}_0(u,v,w)\ \exp\left[j2\pi\left(ul+vm+wn\right)\right]\ du\, dv\, dw \\ \text{where, } \mathcal{V}_0(u,v,w) = \exp\left(-j2\pi w\right)\ \mathcal{V}(u,v,w) \end{array}\right\} \quad \ldots (86)$$

The modified visibility $\mathcal{V}_0(u,v,w)$ is actually the observed visibility having no phase compensation for the delay distance w. It is the visibility with reference to the vertical direction. The relation between the 3D image volume $F(u,v,w)$ and the intensity distribution $I(l,m)$ is given as:

$$F(u,v,w) = \frac{I(l,m)}{\sqrt{1-l^2-m^2}}\delta\left(l^2+m^2+n^2-1\right) \quad \ldots (87)$$

WF Imaging: Non-Coplanar Baselines-IV

Since $l^2 + m^2 + n^2 = 1$, the delta function $\delta(l^2 + m^2 + n^2 - 1)$ exists on a spherical surface of unit radius. This implies $F(u,v,w)$ is empty every where except on this surface of the celestial sphere. Hence the correct intensity distribution is $I(l,m)/n$ which is the value of $F(u,v,w)$ on this unit surface. If δ_0 is the reference declination and $\Delta\alpha$ is the offset from right ascension, we may express the l,m,n coordinates as shown below:

$$\left.\begin{aligned} l &= \cos\delta\ \sin\Delta\alpha \\ m &= \sin\delta\ \cos\delta_0 - \cos\delta\ \sin\delta_0 \cos\Delta\alpha \\ n &= \sin\delta\ \sin\delta_0 + \cos\delta\ \cos\delta_0\ \cos\Delta\alpha \end{aligned}\right\} \quad \ldots (88)$$

The entire imaging process is now same as conventional imaging method. The only difference is we have to deal in 3D with the effects of finite sampling, dirty beam (called ***dirty ball beam***), maximum and minimum baselines, deconvolution etc. However, these are not straight forward and consumes lots of computing power.

Observing Spectral Lines

Line emissions occur under circumstances. For example, hydrogen atom generates a 21cm line at a frequency of 1420.405 MHz due to a transition in hyperfine levels of its ground state. The observed line widths are due to Doppler shifts from different directional motions of particles within the gas like thermal motion. The gas volume itself may be moving away from the observer. Hence the spectral lines are broadened as well as their observed frequencies are different from rest frequency (emission frequency). Additionally, the spectral line also has a natural width of its own imposed by the uncertainty principle, which however is more or less dominated by the processes mentioned before. Systematic rotation and of gas clouds and expansions can significantly deviate the lines from their expected positions.

The observation of spectral lines require higher resolution in frequency to resolve the lines. Hence the number of received channels are generally increased in the range 100 to 1000. Calibration is performed over the entire band-pass response of the instrument which is later subtracted from the spectral line data (containing continuum data from other sources). The left over is the pure spectral line data. In the following sections, we explain these processes step by step.

Obs. Spec. Lines: Rest vs. Obs. Frqs.-I

The rest frequency (emitted frequency) $\nu_{\rm rest}$ can be different from the observed $\nu_{\rm obs}$ because of relative motion between the source and observer. These are related with the relative velocities $\vec{v}_{\rm radio}$ for radio and $\vec{v}_{\rm optical}$ for optical (between the source and the observer) as expressed below in Eqs. (89) and (90), where c is the speed of light.

$$\frac{|\vec{v}_{\rm radio}|}{c} = \frac{\nu_{\rm rest} - \nu_{\rm obs}}{\nu_{\rm rest}} \quad \ldots (89)$$

$$\frac{|\vec{v}_{\rm optical}|}{c} = \frac{\nu_{\rm rest} - \nu_{\rm obs}}{\nu_{\rm obs}} \quad \ldots (90)$$

The above relationships are valid if the two conditions are satisfied:

(i) Relative velocity amplitude is much less than c.

(ii) Angle between the velocity vector and the radiation wave vector is much less than $\pi/2$.

The above velocities are defined with respect to the chosen rest frame of observation which are tabulated next.

Obs. Spec. Lines: Rest vs. Obs. Frqs.-II

Rest Frames and maximum relative velocity amplitudes (IAU).

Rest Frame	**Velocity** $\lvert\vec{v}_{\rm radio}\rvert$
Topocentric (no corrections)	0 km/s
Geocentric (Earth rotation)	< 0.5 km/s
E/M Barycentric (Earth/Moon barycenter)	< 0.013 km/s
Heliocentric (Earth around Sun)	< 30 km/s
SS Barycentric (Sun/planets barycenter)	< 0.012 km/s
Local Standard of Rest (Sun peculiar motion)	< 20 km/s
Galactocentric (Galactic rotation)	< 300 km/s

The position of the observer is topocentric which requires no correction. However, in most of the cases, the observer would like to use a different rest frame like the local standard of rest. Hence, he has to compensate for the velocities of Geocentric, E/M Barycentric, Heliocentric, SS Barycentric and local standard of rest from above. The exact velocity values depend on (*i*) geocentric latitude of the observer, (*ii*) source equatorial coordinates, (*iii*) source ecliptic coordinates, (*iv*) Sun's longitude, (*v*) source hour angle, etc.

Obs. Spec. Lines: Doppler Tracking

Due to Earth rotation, radial velocity $\vec{v}_{\text{rad}}$ keeps changing. Hence, apparent frequency of spectral line continuously changes. In 12 hrs., it may vary ±0.5 km/s. Thus, spectral line drifts across observation band. Time integration broadens the line and decrease its peak. To avoid it, observation frequency is changed continuously so that the line appears in same channel of frequency band. It is known as ***Doppler tracking***. Wide band-widths with negligible integration time can be used to avoid Doppler tracking. Frequency shifts are adjusted during data processing.

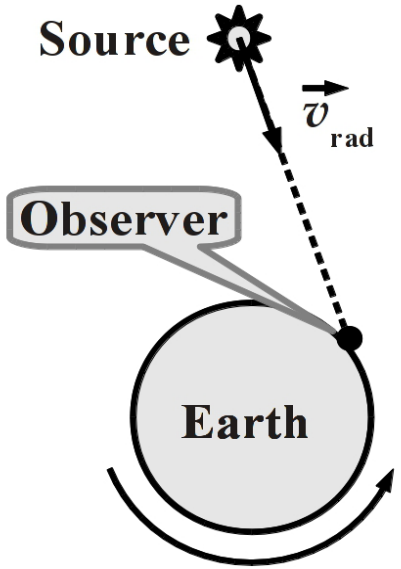

Change of radial velocity between the source and observer due to Earth rotation.

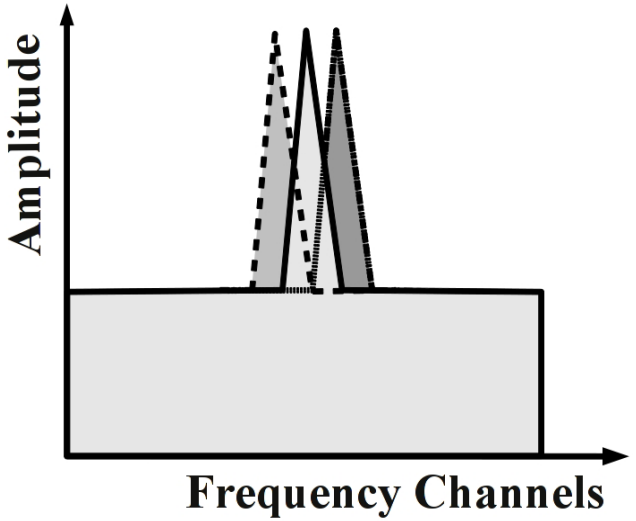

Doppler shifts results in movement of the spectral line across the frequency channels.

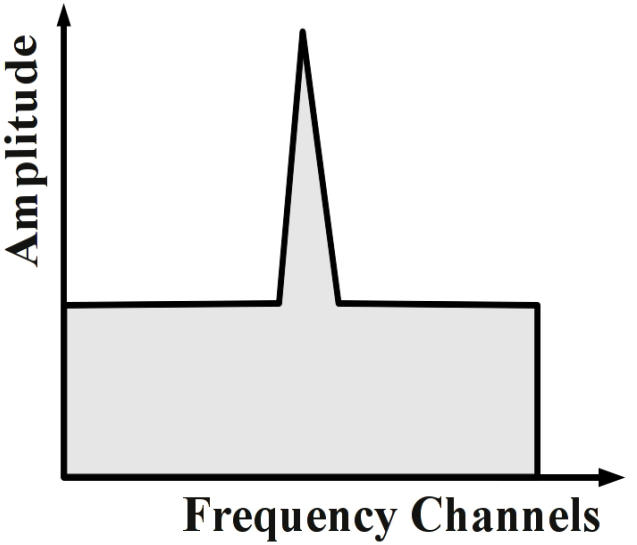

Corrections applied in post processing.

Obs. Spec. Lines: Gain Calibration

The total response of the telescope must be known to determine the true visibilities $\mathcal{V}(\nu,t)$ as a function of frequency and time t from the observed visibilities $\mathcal{V}_{\rm obs}(\nu,t)$ as shown below, where $G(\nu,t)$ is the complex gain of the system.

$$\mathcal{V}_{\rm obs}(\nu,t) = G(\nu,t)\,\mathcal{V}(\nu,t) \quad \ldots (91)$$

$G(\nu,t)$ can be split into two components: (*i*) an overall complex gain $G'(\nu,t)$ for a reference RF within the observing band which varies with time, and (*ii*) gain variations $B(\nu,t)$ across channels (IF bandshape) as shown below. Hence the telescope gain is a combination of RF gain calibration and IF band-shape.

$$G(\nu,t) = G'(t)\,B(\nu,t) \quad \ldots (92)$$

The gain calibration is similar to that for continuum observations. An unresolved source (calibrator) near the direction of the source is observed to estimate the gains of individual antennas in an array. For N antennas, we estimate N amplitudes and N phases from which all the visibilities can be calibrated. Certain number of spectral channels are averaged to improve the SNR. The calibration also takes care of atmospheric offsets, since the calibrator is chosen in a direction close to the source.

Obs. Spec. Lines: Band-pass Calibration-I

A bright unresolved source containing no spectral lines can be used for band-pass (band-shape) calibration. However, the calibrator source need not be in a direction close to the target source. We may simply apply the folllowing equation for obtaining $B(\nu,t)$, where $B_{\rm obs}(\nu,t)$ is the observed flux-density variations across the band-shape and $S_{\rm cal}$ is the flux-density of the calibrator source (which is known).

$$B(\nu,t) = \frac{B_{\rm obs}(\nu,t)}{S_{\rm cal}} \quad \ldots (93)$$

This however requires a very high SNR such that the corrected spectrum is not degraded. In other words, one should obtain an intrinsically flat spectrum band-shape. In general, one of the two methods are employed in band-pass calibration:

(i) Position Switching.
(ii) Frequency Switching.

(i) **Position Switching:**

- This is done while observing the target source. Intermittently, the telescope is pointed to the calibrator once within 20 mins to an hour depending on the stability of telescope properties.

Obs. Spec. Lines: Band-pass Calibration-II

(*ii*) **Frequency Switching:**

- Presence of gases may introduce spectral line features in the path of the calibrator depending on the frequency of interest. Example of such a gas could be the ***Galactic neutral Hydrogen*** (HI). Again if the target source is brighter than the calibrator, the later has to be observed for more duration (for the same settings of the telescope) for achieving good SNR. Under these conditions, it may be useful to note the response at neighboring frequencies outside the spectral line. These adjacent band-shapes may be used for calibration of the observed spectrum. Hence, by switching between the adjacent frequencies one can estimate the band-shape which is largely decided by the shape of the base-band filter.

Obs. Spec. Lines: Spectrum Smoothening-I

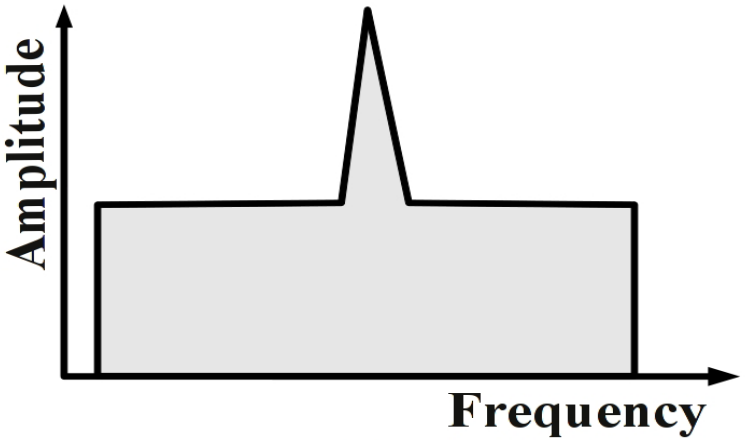

Expected spectrum.

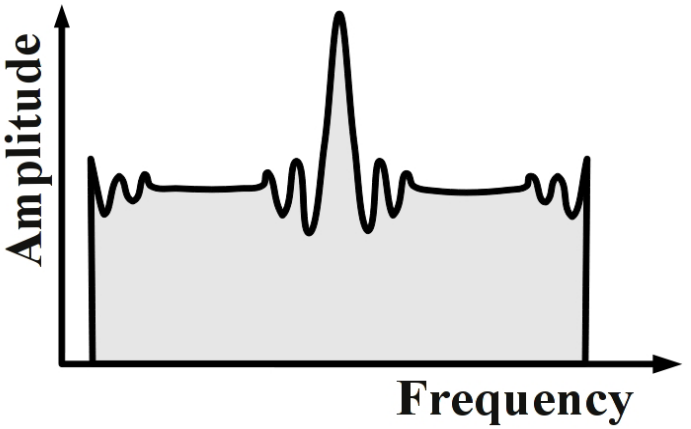

Measured spectrum.

Due to limited number of correlation products and finite time we cannot measure an infinite number of Fourier components. In other words, a spectrum having a bandwidth $\Delta\nu$ and N channels is a result of cross-correlations between signals sampled at time intervals of $\tau = 1/\Delta\nu$ in the range $-N\tau$ to $(N\text{-}1)\tau$ produced by the telescope. It is equivalent to truncation in time range by a Rectangular window, due to to Gibbs phenomenon. Ringing effect is seen on sharp edges. It may be viewed as convolution of the true spectrum with a sinc function.

Obs. Spec. Lines: Spectrum Smoothening-I

Several different smoothing functions can be used to minimize this unwanted ringing, but at the expense of spectral resolution. The most commonly used is the Hanning window which helps in bringing down the first side-lobes from 22% to less than 3%.

Due to emission from nearby sources in the field of view towards the target source, the data often contain continuum signals. This complicates the detection and analysis of line data. Hence these unwanted signatures must be removed.

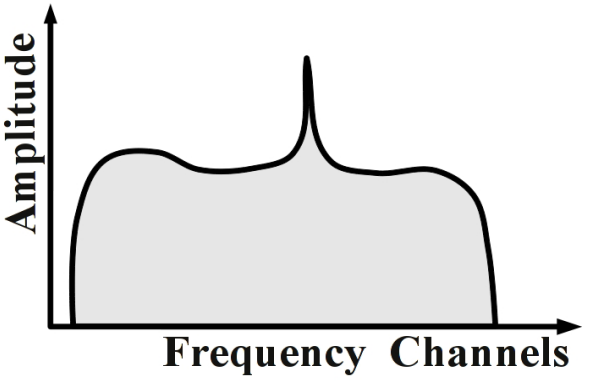

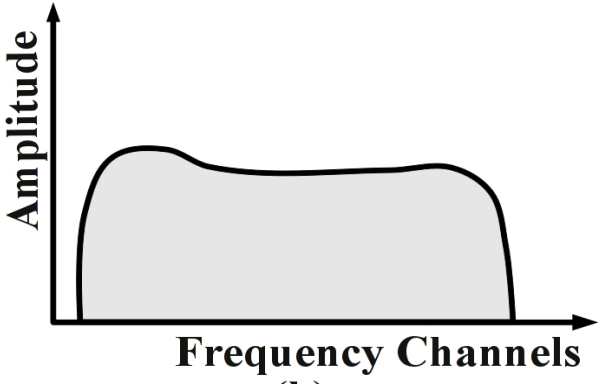

A model of continuum is created using frequency channels having no line features as shown on left. This model is subtracted from all channels and the residue contains only the spectral information as shown below:

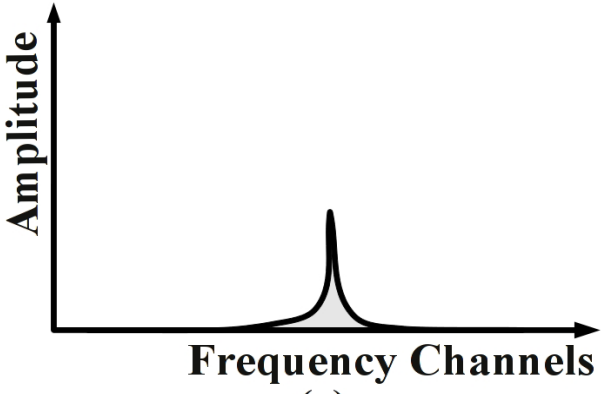

Spectral Line Features: Basic Ideas

A spectral line is a extremely narrow, but due to internal motions within the gas volume, the line-width increases. It becomes a function of the velocity distribution of the particles within the gas volume. The velocity variations are see as frequency variations in radio telescope data. These are converted into a velocity profile before plotting. Thus we have three coordinates: two for position and one for velocity. These plots are know as ***spectral data cubes*** as shown on right. One can make slices in a RA-Dec plane at fixed velocities to see the spread for that velocity.

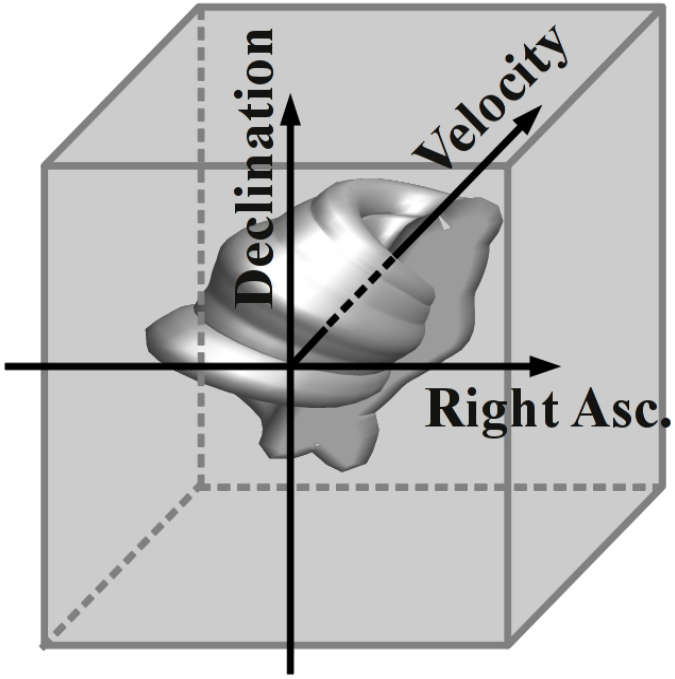

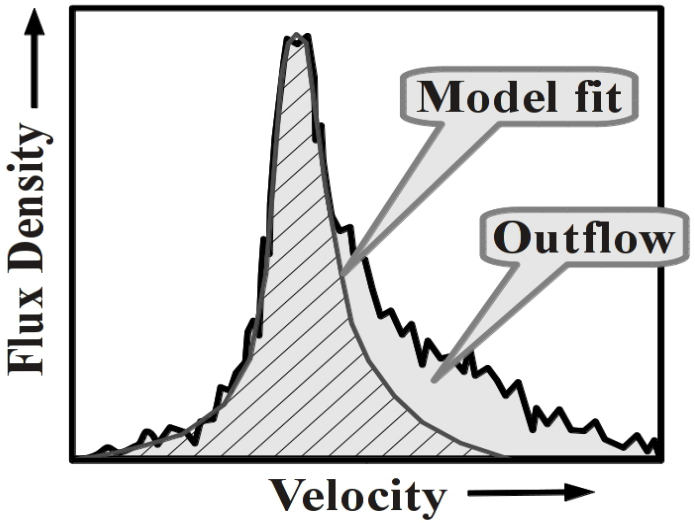

The flux-density of a hot gas distribution if plotted against velocity (as shown on left), one can fit a model curve to find outflow of gases if any. The hatched region shows the line broadening due to thermal motion of the gas particles. The excess velocity is determined from the gray region (no-hatchings) on the right.

Assignment Problems-I

1. Why is the approximated van Cittert-Zernike equation so important in conventional imaging? What are its drawbacks?

2. Why do you need to calibrate the data before imaging?

3. What is meant by flagging bad data?

4. What are the significance of long term and short term calibrations?

5. What is difference between a gain calibrator and phase calibrator?

6. Why do you require a point source for phase calibrations?

7. Under what circumstances a gain calibrator can be used as phase calibrator? Explain with reasoning.

8. What is meant by (*i*) phase closure and (*ii*) gain closure in selfcalibration?

9. How does a redundant baseline array help in self-calibration?

Assignment Problems-II

10. What is reason behind applying weights to the visibilities during an imaging procedure?

11. What is the difference between natural weights and uniform weights?

12. Why are the tapered weights preferable against natural and uniform weights?

13. Why is the robust weights most preferable?

14. Explain the purpose of gridding the visibilities using uniform spacing across the *u*-*v* plane?

15. Explain the gridding procedure in one dimension using a figure.

16. What should be the ideal shape of the Fourier transform $\overline{C}(l,m)$ of the convolution function $C(u,v)$?

17. How does expressing the convolution function $C(u,v)$ as a product of two functions $C_1(u)C_2(v)$ help in gridding process?

Assignment Problems-III

18. What is meant by dirty image?

19. Why do you need to perform deconvolution on the dirty image?

20. Using a diagram, explain the basic CLEAN deconvolution algorithm.

21. What is meant by band-width smearing? Using a diagram explain its effects on the *u*-*v* plane.

22. What is meant by multi frequency synthesis? What are its advantages?

23. What is the basic difference between conventional imaging and wide-field Imaging?

24. What is meant by short spacing problem, especially in wide-field imaging?

25. Using a diagram explain the negative bowl effect on the synthesized beam.

Assignment Problems-IV

26. Using a diagram show the data analogies between a single dish and a multiplicative interferometer.

27. Using a diagram explain the process of generating *u*-*v* data using a single dish in wide-field imaging.

28. Using a diagram explain how does the negative bowl effect is removed by combining single dish data with interferometer data.

29. Using a diagram explain the principle of mosaicking.

30. What is the difference between coplanar and non-coplanar baselines?

31. Explain the phase problem arising due to the *w* component while observing a source at the zenith using an interferometer having two antennas at different heights.

32. What are differences between a dirty-beam and a dirty-ball-beam? Where are they used ?

Assignment Problems-V

33. What are spectral lines? State some of the possible reasons for spectral broadening.

34. Explain the meaning of rest and observing frequencies of a spectral line.

35. Give reasons for the Doppler tracking in spectral line observation.

36. What is meant by band-pass calibration? Explain with a suitable diagram.

37. Why do you need to subtract the continuum from the data and how is it done? Explain with a diagram.

38. Explain the structure of a data cube using a 3D diagram.

THANK YOU